

1

Snow Interception Relationships with 2 Meteorology and Canopy Structure in a 3 Subalpine Forest

4

5 **Authors:**

6 A. Cebulski¹ (ORCID ID - 0000-0001-7910-5056)

7 J.W. Pomeroy¹ (ORCID ID - 0000-0002-4782-7457)

8 ¹Centre for Hydrology, University of Saskatchewan, Canmore, Canada

9 **Corresponding Author:** A. Cebulski, alexcebulski@gmail.com

10 **Abstract:** Snow accumulation models differ in how snow interception and ablation processes
11 are represented and thus their application to diverse climates and forest types is uncertain.
12 Existing parameterizations of initial snow interception before unloading include inherently
13 coupled canopy snow accumulation and ablation processes. This leads to difficulty in di-
14 agnosing processes and adding possible errors to simulations when incorporated as canopy
15 interception routines in models that already account for canopy snow ablation. This study
16 evaluates the theory underpinning parameterizations of initial snow interception using high-
17 temporal resolution and fine-scale measurements of throughfall for events with minimal snow
18 ablation and redistribution in both the canopy and on the ground. The relationship between
19 these throughfall measurements, event meteorology, and a novel lidar-based canopy structure
20 measurement are assessed in two subalpine forest plots in the Canadian Rockies. Contrary
21 to existing theories, no association of canopy snow load or air temperature with interception

efficiency was observed. Instead, canopy structure emerged as the primary factor governing snow accumulation. A wind-driven snowfall event demonstrated that non-vertical hydrometeor trajectories can significantly increase snow-leaf contact area, thereby enhancing initial interception before ablation. Prediction of interception efficiency for this event improved dramatically when adjusted for hydrometeor trajectory angle based on a wind speed at one-third of the canopy height. Snow-leaf contact area showed a high sensitivity to wind speed, increasing by up to 95% with a 1 m s^{-1} wind speed. The study proposes a new parameterization that calculates throughfall, independent of processes that ablate snow from the canopy, as a function of snow-leaf contact area adjusted for hydrometeor trajectory angle. This new parameterization successfully estimated subcanopy snow accumulation for a snowfall event at two forest plots measured using lidar and snow surveys. By separating canopy snow ablation from snow interception processes, this new model offers potentially improved prediction of subcanopy snow accumulation when combined with canopy snow ablation parameterizations.

Keywords: snow interception, throughfall, ablation, forest, snowpack, lidar, process-based modelling

1 Introduction

Over half of North America's snow-covered zone is covered by forests (Kim et al., 2017), significantly impacting the accumulation and redistribution of snowpacks and subsequent snowmelt runoff. Essery et al. (2003) estimated that 25–45% of annual snowfall may be lost to the atmosphere due to sublimation of snow intercepted in forest canopies globally. Snow intercepted in the canopy can sublimate and melt at much higher rates than the subcanopy snowpack (Katsushima et al., 2023; Lundberg & Halladin, 1994; Pomeroy et al., 1998), reducing the amount of snow available for runoff. Vegetation structure is one of the primary factors controlling the partitioning of snowfall into throughfall and interception (Hedstrom & Pomeroy, 1998; Storck et al., 2002), and thus governs the quantity of snow subject to sublimation from the canopy. However, forest thinning efforts aimed at limiting sublimation losses to increase

48 snowmelt runoff do not always lead to a corresponding increase in spring streamflow (Golding
49 & Swanson, 1978; Harpold et al., 2020; Pomeroy et al., 2012; Troendle, 1983). This may be
50 due to increased ablation rates when forest cover is reduced, desynchronization of snowmelt,
51 and sub-surface hydrology interactions (Ellis et al., 2013; Musselman et al., 2015; Pomeroy et
52 al., 1997; Safa et al., 2021; Varhola et al., 2010). Due to the significant impact of forest cover
53 on snow accumulation and ablation, and sparse or absent monitoring networks for subcanopy
54 snow accumulation (Rittger et al., 2020; Vionnet et al., 2021), land management, ecological
55 conservation and water resource decisions rely on robust models of snow redistribution to
56 estimate past, current and future subcanopy snowpacks.

57 Hedstrom & Pomeroy (1998), working in the cold continental boreal forest, proposed that
58 initial snow interception efficiency was controlled by the maximum canopy load which itself
59 was a function of leaf area index and new snow density. Unloading was found to be an expo-
60 nential function of time and observed only days or weeks after the interception event. Storck
61 et al. (2002), working in temperate coastal forests, emphasized the role of leaf area index
62 and air temperature in controlling the maximum canopy snow load. Gelfan et al. (2004)
63 demonstrated accurate subcanopy snowpack simulations at study sites in Russia by treating
64 the Hedstrom & Pomeroy (1998) and Storck et al. (2002) parameterizations separately while
65 using a step-based function to choose either parameterization based on air temperature. A
66 similar parameterization in the Cold Regions Hydrological Model (Pomeroy et al., 2022) has
67 shown strong performance at sites across Canada, northern United States, Switzerland, and
68 Spain. However, overestimation of subcanopy snow accumulation was reported by Lundquist
69 et al. (2021) and Lumbrazo et al. (2022) when combining the Hedstrom & Pomeroy (1998)
70 routine with ablation parameterizations from different studies (e.g., Roesch et al., 2001). The
71 coupling of ablation processes within existing snow interception models (Hedstrom & Pomeroy,
72 1998; Storck et al., 2002) may contribute to overestimates of throughfall, canopy snow unload-
73 ing, and canopy snow melt when combined with other canopy snow ablation parameterizations
74 (Cebulski & Pomeroy, 2024). Additional observations of snow interception that exclude abla-
75 tion processes could help determine the applicability of the interception theories proposed by

76 Hedstrom & Pomeroy (1998) and Storck et al. (2002). Hedstrom & Pomeroy's (1998) theory
77 also suggests that moderate wind speeds, which can result in more horizontal hydrometeor tra-
78 jectories and increase the snow-leaf contact area and interception efficiency at the plot scale.
79 This association has also been shown in rainfall interception studies to decrease throughfall
80 of rain (Herwitz & Slye, 1995; Van Stan et al., 2011). Despite this importance for rainfall,
81 the relationship proposed by Hedstrom & Pomeroy (1998), has typically not been included in
82 snow accumulation models (Clark et al., 2020; Mahat & Tarboton, 2014) as empirical testing
83 of this relationship is lacking.

84 The objective of this paper is to evaluate the theories underlying existing snow interception
85 models using high spatial and temporal resolution measurements of subcanopy snow accumu-
86 lation for events with minimal canopy snow ablation. These new observations are investigated
87 to address the following research questions:

- 88 1. Are the existing theories regarding the relationships between meteorology and forest
89 structure and initial snow interception supported by in-situ observations?
- 90 2. Is snow interception influenced by non-vertical hydrometeor trajectory angles over a
91 wind-driven snowfall event?
- 92 3. To what extent can these findings inform the development of a new parameterization for
93 snow interception?

94 **2 Theory**

95 **2.1 Snow interception**

96 The change in canopy snow load over time, $\frac{dL}{dt}$ ($\text{kg m}^{-2} \text{ s}^{-1}$), can be estimated from the mass
97 balance:

$$\frac{dL}{dt} = q_{sf} + q_{ros} - q_{tf} - q_{unld} - q_{drip} - q_{wind}^{veg} - q_{sub}^{veg} \quad (1)$$

where q_{sf} is the snowfall rate ($\text{kg m}^{-2} \text{ s}^{-1}$), q_{ros} ($\text{kg m}^{-2} \text{ s}^{-1}$) is the rate of rainfall falling on snow intercepted in the canopy, q_{tf} ($\text{kg m}^{-2} \text{ s}^{-1}$) is the throughfall rate ($\text{kg m}^{-2} \text{ s}^{-1}$), q_{unld} is the canopy snow unloading rate ($\text{kg m}^{-2} \text{ s}^{-1}$), q_{drip} is the canopy snow drip rate due to canopy snowmelt ($\text{kg m}^{-2} \text{ s}^{-1}$), q_{wind}^{veg} is the wind transport rate in or out of the control volume ($\text{kg m}^{-2} \text{ s}^{-1}$), and q_{sub}^{veg} is the intercepted snow sublimation rate ($\text{kg m}^{-2} \text{ s}^{-1}$). During periods with low air temperatures and low wind speeds, q_{ros} , q_{unld} , q_{drip} , q_{wind}^{veg} , and q_{sub}^{veg} can be assumed negligible. Figure 1 in Cebulski & Pomeroy (2024) presents a visual representation of this mass balance.

Interception efficiency, $\frac{I}{P}$ (-), which is the fraction of snowfall intercepted over Δt before ablation, can be calculated as:

$$\frac{I}{P} = \frac{\Delta L}{q_{sf}\Delta t} \quad (2)$$

and throughfall, q_{tf} can be calculated as:

$$q_{tf} = \left(1 - \frac{I}{P}\right) \cdot q_{sf} \quad (3)$$

2.2 Hydrometeor trajectory angle

The trajectory angle, θ_h of a hydrometeor as the departure in degrees ($^\circ$) from a vertical plane, is shown in Herwitz & Slye (1995) to be calculated as:

$$\theta_h = \arctan\left(\frac{x_h(u_z)}{v_h(D_h)}\right) * \frac{180}{\pi} \quad (4)$$

where $v_h(D_h)$ is the terminal fall velocity of the hydrometeor (m s^{-1}), which is a function of the hydrometeor diameter, D_h and $x_h(u_z)$ is the horizontal velocity of the hydrometeor (m s^{-1}) which is a function of the within canopy wind speed, u_z at height above ground, z . This assumes the hydrometeors are following fluid points in the atmosphere.

¹¹⁶ **3 Data and methods**

¹¹⁷ **3.1 Study site**

¹¹⁸ This study was conducted at Fortress Mountain Research Basin (FMRB), Alberta, Canada,
¹¹⁹ -115° W, 51° N, a continental headwater basin in the Canadian Rockies (Figure 1). Data from
¹²⁰ this study was collected between October 2021 and July 2023 within and surrounding two
¹²¹ forest plots adjacent to the FMRB Powerline Station (PWL) and Forest Tower Station (FT)
¹²² at ~2100 m above sea level as shown in Figure 1. The average annual precipitation at PWL
¹²³ Station from 2013 to 2023 was 1045 mm, with the peak annual snow water equivalent (SWE)
¹²⁴ reaching 465 kg m⁻², typically occurring in late April. The PWL and FT forest plots include
¹²⁵ discontinuous stands of 70% subalpine fir (*Abies lasiocarpa*) and 30% Engelmann spruce (*Picea*
¹²⁶ *engelmannii*) (Langs et al., 2020). The PWL plot is located 120 m to the northwest of FT
¹²⁷ station and contains a forest clearing with a diameter of ~12 m, surrounded by a closed canopy.
¹²⁸ The canopy coverages of the two forest plots are 0.51 and 0.29 and the winter leaf area indices
¹²⁹ are 2.07 and 1.66 for PWL and FT respectively. The average height of the canopy surrounding
¹³⁰ the plot to the east of the PWL station is 10.5 m and surrounding the forest plot around the
¹³¹ FT Station is 7.1 m. The forest of the FT plot has a discontinuous canopy without artificial
¹³² clearings. In August of 1936, the majority of vegetation in FMRB burned during a large forest
¹³³ fire that affected most of the Kananaskis Valley (Fryer et al., 1988). Following the fire, the
¹³⁴ forest within the PWL and FT forest plots has naturally regenerated, though some trees have
¹³⁵ been removed for road clearing and creation of a snow study plot.

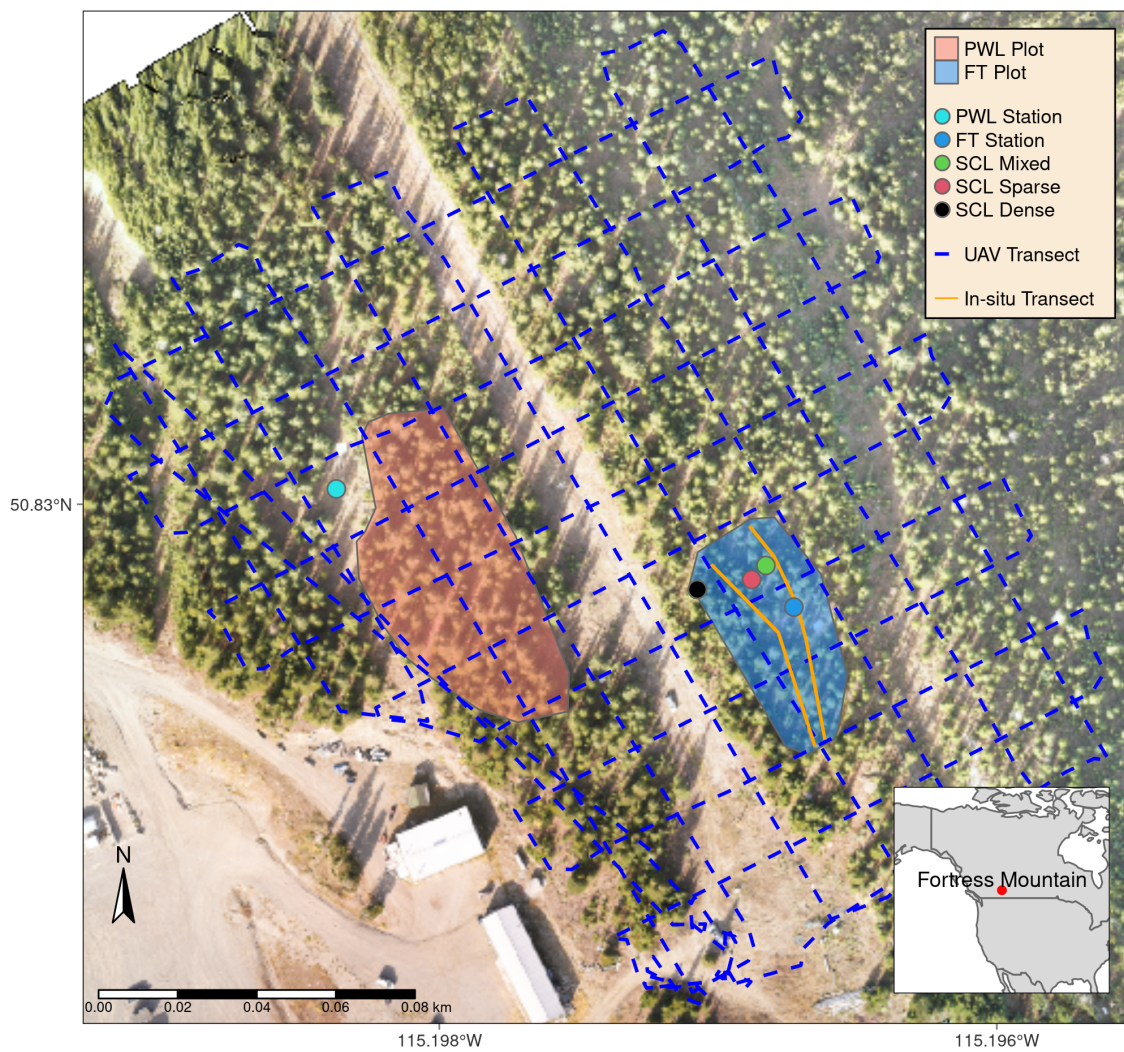


Figure 1: Map showing the location of forest plots, flux towers, subcanopy lysimeter instruments (SCL), and survey transects. The inset map on the lower right shows the regional location of Fortress Mountain Research basin.

¹³⁶ **3.2 Meteorological measurements**

¹³⁷ Measurements of air temperature and relative humidity (Vaisala model HMP155A), wind speed
¹³⁸ and direction (RM Young model 86000 2-D ultrasonic anemometer) were made 4.3 m above the
¹³⁹ ground at FT station (Figure 1). Wind speed measurements from a 3-cup anemometer (Met
¹⁴⁰ One model 014A), installed adjacent to the 2-D ultrasonic anemometer at 4.3 m, were used for
¹⁴¹ gap filling wind speed. Additional wind speed measurements were collected by two 3D sonic
¹⁴² anemometers (Campbell Scientific CSAT3) installed at 2 m (raised to 3 m February 2022) and
¹⁴³ 13.5 m above the ground at FT station. Average wind speeds at these three heights were found
¹⁴⁴ to follow a logarithmic relationship. Thus, a wind profile was fitted to these measurements
¹⁴⁵ using the Prandtl-von Kármán log-linear relationship:

$$\bar{u} = \frac{u_*}{k} \ln\left(\frac{z - d_0}{z_0}\right) \quad (5)$$

¹⁴⁶ where \bar{u} is average wind speed (m s^{-1}) at height, z (m) above the ground, u_* is the friction
¹⁴⁷ velocity (m s^{-1}), d_0 is the displacement height (m), z_0 is the roughness length of momentum
¹⁴⁸ (m), and k is the dimensionless von Kármán Constant (0.4).

¹⁴⁹ Using wind speed measurements at three heights at FT station, collected during events when
¹⁵⁰ the instruments were confirmed to be free of snow, the function ‘optim’ from the ‘stats’ R
¹⁵¹ package (R Core Team, 2024) was used to estimate the values d_0 and z_0 for Equation 5 that
¹⁵² best fit the observed mean wind speed. The parameters found for the wind speed profile
¹⁵³ include a d_0 of 0.58 m and z_0 of 0.50 m. See the supporting information for more information
¹⁵⁴ on the development and testing of the wind profile.

¹⁵⁵ At PWL station, the snowfall rate was measured by an Alter-shielded OTT Pluvio weighing
¹⁵⁶ precipitation gauge 2.6 m above ground, corrected for undercatch following phase correction
¹⁵⁷ by Harder & Pomeroy (2013) and catch efficiency by Smith (2007). Wind speed for undercatch
¹⁵⁸ correction was measured by a 3-cup anemometer (Met One model 014A) at a height of 2.6 m at
¹⁵⁹ PWL station. An optical disdrometer (OTT Parsivel2) provided measurements of hydrometeor

¹⁶⁰ particle size and vertical velocity. All measurements were recorded at 15-min intervals using
¹⁶¹ Campbell Scientific dataloggers, except the Parsivel2 which was recorded at 1-minute intervals
¹⁶² by an onsite computer.

¹⁶³ **3.3 Lysimeter measurements**

¹⁶⁴ Three subcanopy lysimeters (SCLs) were installed surrounding the FT Station (Figure 1) to
¹⁶⁵ provide 15-minute interval measurements of throughfall as in MacDonald (2010). Figure 2
¹⁶⁶ shows the three SCLs which consisted of a plastic horse-watering trough with an opening of
¹⁶⁷ 0.9 m² and depth of 20 cm suspended from a load cell (Intertechnology 9363-D3-75-20T1)
¹⁶⁸ attached to an aluminum pipe connected between two trees. For 26 distinct snowfall events,
¹⁶⁹ where canopy snow ablation rates were deemed negligible, snow captured in the SCLs was
¹⁷⁰ assumed to be throughfall. The throughfall rate, q_{tf} , was calculated by dividing the weight
¹⁷¹ of snow in the SCL by the cross-sectional area of the SCL opening and determining the rate
¹⁷² of change at 15-minute intervals. Canopy snow load was estimated at the same 15-minute
¹⁷³ intervals during these events using Equation 1 and incorporating measurements of q_{tf} from
¹⁷⁴ the SCLs and q_{sf} from the PWL snowfall gauge. Rates of q_{ros} , q_{unld} , q_{drip} , q_{wind}^{veg} , and q_{sub}^{veg}
¹⁷⁵ were assumed to be zero for these periods. Interception efficiency was also calculated for
¹⁷⁶ these intervals using Equation 2. Timelapse imagery, mass change on a weighed tree lysimeter
¹⁷⁷ “hanging tree” (Pomeroy & Schmidt, 1993) and in-situ observations were used to ensure the
¹⁷⁸ ablation of snow intercepted in the canopy was minimal over each interval. Additionally,
¹⁷⁹ the q_{tf} measurements were filtered to include observations with a snowfall rate $> 0 \text{ kg m}^{-2}$
¹⁸⁰ hr⁻¹, throughfall rate $> 0.05 \text{ kg m}^{-2} \text{ hr}^{-1}$ and a snowfall rate greater than the SCL measured
¹⁸¹ throughfall rate to minimize observations with unloading. The weighed tree lysimeter, a live
¹⁸² subalpine fir (*Abies lasiocarpa*) tree suspended from a load cell (Artech S-Type 20210-100)
¹⁸³ measured the weight of canopy snow load (kg). This weight was scaled to an areal estimate of
¹⁸⁴ canopy snow load (L , kg m⁻²) using measurements of areal throughfall (kg m⁻²) from manual
¹⁸⁵ snow surveys and snowfall from the PWL Station snowfall gauge (see description of method
¹⁸⁶ in Pomeroy & Schmidt, 1993). The canopy structure surrounding three SCLs is shown in

¹⁸⁷ Figure 2 and was measured using hemispherical photography (Nikon Coolpix 4500 and EC-F8
¹⁸⁸ hemispherical lens) and the hemispheR R package Chianucci & Macek (2023). The leaf area
¹⁸⁹ index and canopy coverage from hemispherical photo analysis is shown in Table 1.

Table 1: Canopy structure of the three subcanopy lysimeters (SCL) located proximal to the FT Station. Leaf area index (LAI) and Canopy Coverage was measured using hemispherical photo analysis with the R package hemispheR.

Name	LAI (-)	Canopy Coverage (-)
Sparse	1.59	0.73
Mixed	1.86	0.78
Closed	2.11	0.82

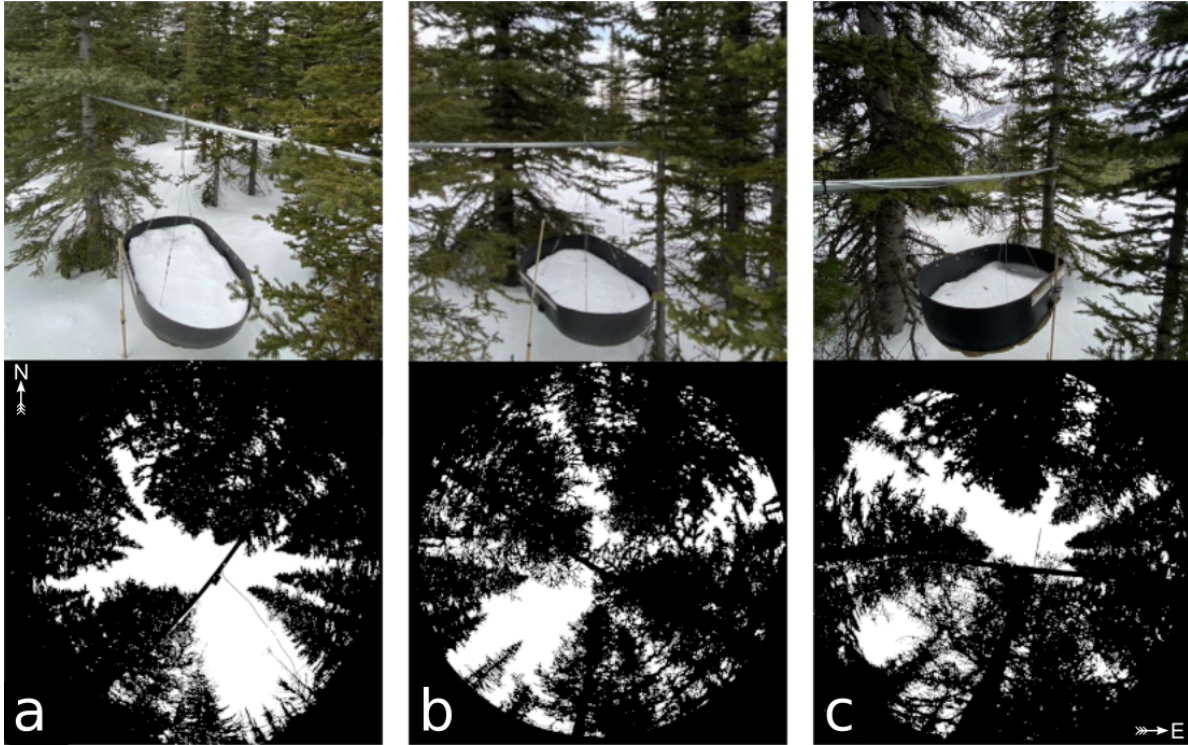


Figure 2: Images of the three subcanopy lysimeters (SCL) and surrounding canopy located in sparse (a), mixed (b), and dense (c) canopy. The top row presents a side view of each SCL and the bottom row shows hemispherical photographs classified using the hemispheR R package. These hemispherical images are oriented with north at the top and have been flipped to provide a view from above (i.e., east is on the right side of each image). See Table 1 for the canopy structure measurements of the canopy above each SCL.

190 3.4 UAV-Lidar data collection and processing

191 The UAV (FreeFly Alta X) payload included a REIGL miniVUX-2 airborne laser scanner,
 192 an Applanix APX-20 inertial measurement unit (IMU) and global navigation satellite system
 193 (GNSS). The UAV was flown 90 m above the ground at a speed of 3 m s^{-1} following the
 194 path shown in Figure 1. A detailed description of the UAV, payload, and flight settings is
 195 provided in the supporting information. The methods outlined by Harder et al. (2020) and
 196 Staines & Pomeroy (2023) were incorporated to reconcile survey lidar, IMU and GNSS data.

197 A systematic vertical bias of up to 6 cm between UAV-lidar flight lines was observed in the
198 resulting point clouds on March 13th and 14th, 2024 and was attributed to IMU position
199 drift. This offset between flight lines was corrected using the BayesStripAlign software v2.24
200 (BayesMap Solutions, 2024). After strip alignment, the mean elevation bias in the point clouds
201 was 0.000 m and the RMS error declined from 0.055 m to 0.038 m on March 13th and changed
202 from 0.033 m to 0.029 m on March 14th. The point cloud density ranged from ~1200 returns m²
203 in sparse forest to ~2200 returns m² in open clearings. Quality control, ground classification,
204 calculation of surface elevation change (subtraction of the two UAV-lidar point clouds), and
205 generation of 0.05 m resolution rasters was conducted using the LAStools software package
206 (LAStools, 2024). Post processing and resampling of raster data to a 0.25 m grid cell resolution
207 was conducted using the ‘Terra’ R package (Hijmans, 2024). More details on the UAV-lidar
208 processing workflow are provided in the supporting information.

209 **3.5 Snow surveys**

210 **3.5.1 In-situ snow depth and density**

211 Twelve in-situ fresh snow surveys (six pre- and post-snowfall event pairs) provided measure-
212 ments of subcanopy throughfall depth and density at 30 locations following the transects shown
213 in Figure 1 to upscale the weighed tree snow load from kg to kg m⁻² as in Pomeroy & Schmidt
214 (1993). Minimal ablation and redistribution of snow was observed between the pre- and post-
215 snowfall surveys. When conditions allowed for a UAV-lidar flight, the in-situ snow surveys
216 were conducted following the UAV-lidar flight to assess the accuracy of the throughfall mea-
217 surements and provide a fresh snow density for the calculation of SWE (kg m⁻²). A 1000 cm³
218 Perla snow density wedge sampler (RIP Cutter, [https://snowmetrics.com/shop/rip-1-cutter-](https://snowmetrics.com/shop/rip-1-cutter-1000-cc/)
219 1000-cc/) was used to measure the density of the fresh snow layer, ρ_{tf} (kg m⁻³) from snow
220 pits. Throughfall depth measurements, ΔHS were converted to SWE using the following
221 equation:

$$\Delta SWE_{tf} = \Delta HS \cdot \overline{\rho_{tf}} \quad (6)$$

222 Differential GNSS rover coordinates, with ± 2.5 cm 3D uncertainty, were taken at each snow
223 sampling location so the locations could be queried later from the UAV-lidar rasters to assess
224 measurement error and were also used as input for the UAV-lidar strip alignment. If a pre-
225 event crust layer was present, the depth of post event fresh snow accumulation above the crust
226 layer was interpreted as throughfall over the event. In the absence of a defined crust layer, the
227 difference in pre- and post-event snow depth to ground was interpreted as event throughfall.

228 **3.5.2 UAV-Lidar snow depth**

229 Two uncrewed aerial vehicle (UAV) lidar surveys were conducted before and after a 24-hour
230 snowfall event that occurred between March 13th and March 14th, 2023 to facilitate the mea-
231 surement of snow accumulation and canopy structure within the FT and PWL forest plots.
232 This period was selected based on two criteria: 1) it provided sufficient cumulative snowfall
233 to result in a low relative error in UAV-lidar measured throughfall, and (2) minimal snow
234 redistribution and ablation was observed, as confirmed by the SCLs, weighed tree, and time-
235 lapse imagery. The change in surface elevation between the two UAV-lidar point clouds was
236 interpreted as the increase in snow accumulation, ΔHS over the snowfall event.

237 **3.6 UAV-Lidar canopy metrics**

238 The canopy structure in the two UAV-lidar point clouds (March 13th and March 14th) was
239 characterized using the voxel ray sampling (VoxRS) methodology for lidar data analysis, as
240 developed by Staines & Pomeroy (2023). This method was chosen for its ability to provide
241 canopy metrics that are less sensitive to the inherent non-uniform nature of lidar sampling data,
242 which often results from beam occlusion in vegetation and leads to reduced points near the
243 ground. Using this method radiation transmittance, $\tau (-)$, was measured across the hemisphere

244 at a 1° step, i.e., azimuth angles ($0^\circ, 1^\circ, \dots, 359^\circ$) and zenith angles ($0^\circ, 1^\circ, \dots, 90^\circ$) for each
245 0.25 m grid cell within the FT and PWL forest plots. The fraction of snow-leaf contact area
246 per unit area of ground proposed by Hedstrom & Pomeroy (1998), and hereafter called leaf
247 contact area (C_p), was then calculated as:

$$C_p(C_c, \theta_h, L) = 1 - \tau \quad (7)$$

$$C_p(C_c, \theta_h, L) = \begin{cases} 1 - \tau, & \text{if } \theta_h > 0^\circ \\ 1 - \tau \approx C_c, & \theta_h = 0^\circ \end{cases} \quad (8)$$

248 where C_p is a function of the canopy coverage C_c , θ_h and L . C_p is approximately equal to
249 canopy coverage (C_c) for vertical snowfall trajectories.

250 **3.7 Statistics and regression models**

251 To determine how forest structure was associated with interception efficiency at different az-
252 imuth and zenith angles over the March 13—14 snowfall event, the entire hemisphere at each
253 grid location was considered. The relationship between interception efficiency and C_p was
254 found to be linear and thus the Pearson Correlation Coefficient, ρ_p was calculated using the
255 ‘stats’ package in R (R Core Team, 2024). The ρ_p was computed between a single raster of
256 interception efficiency and each of the 32,760 rasters of C_p , representing locations across the
257 hemisphere (azimuth [$0^\circ, 1^\circ, \dots, 359^\circ$], zenith angle [$0^\circ, 1^\circ, \dots, 90^\circ$]) at 0.25 m grid cells spanning
258 the FT and PWL forest plots.

259 Linear and non-linear regression models were developed to assess relationships in the observed
260 data. Linear models were fitted using ordinary least squares regression via the ‘lm’ function
261 from the R ‘stats’ package (R Core Team, 2024) to analyze two relationships: (1) between
262 interception efficiency and meteorological variables and (2) between interception efficiency and
263 leaf contact area. The latter was forced through the origin based on the theoretical justification

that the dependent variable should be zero when the independent variable is zero. Kozak & Kozak (1995) noted, the default R^2 value provided for least squares models forced through the origin by many statistical packages can be misleading. Therefore, these R^2 values were adjusted using Equation 10 in Kozak & Kozak (1995). Non-linear models were fitted to investigate the relationship of leaf contact area with simulated trajectory angle using non-linear least squares regression via the ‘nls’ function in ‘stats’ package in R.

4 Results

4.1 The influence of meteorology on snow interception

Canopy snow load was estimated for 26 snowfall events and increased linearly with cumulative event snowfall without evidence of reaching a maximum (Figure 3). Over these events, air temperature ranged from -24.5°C to 1°C, wind speeds at 4.3 m height ranged from calm to 4.6 m s^{-1} (Table 2), and wind direction was predominately from the southwest during snowfall (Figure 4). Missing canopy snow load measurements in Figure 3 for certain troughs during specific events was caused by damage to the subcanopy lysimeter wiring due to animals and heavy snow loads.

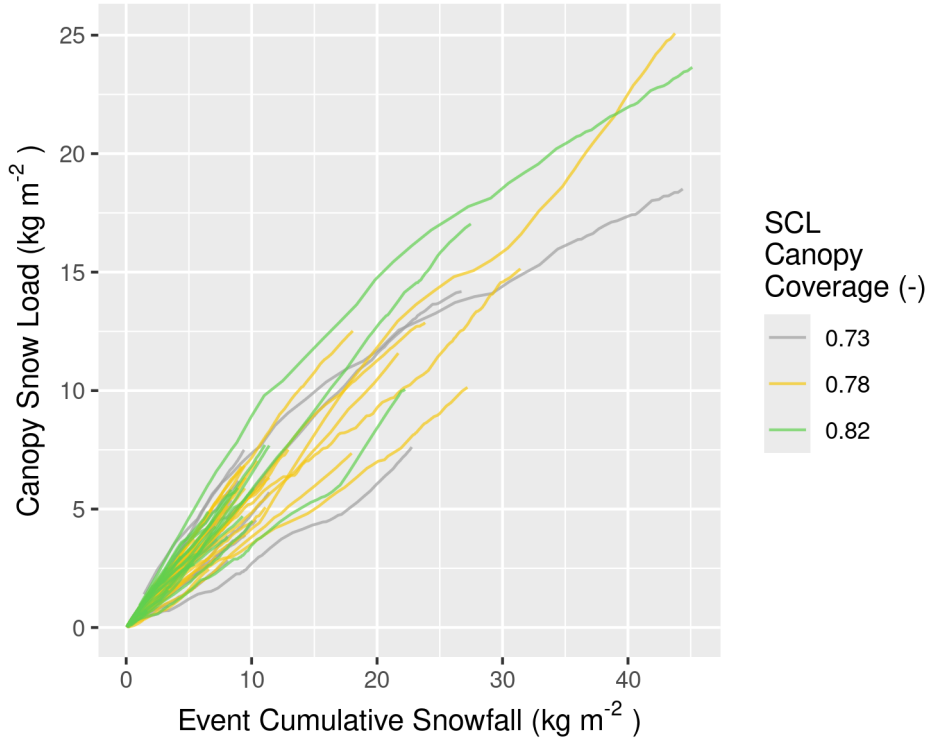


Figure 3: Plot showing the cumulative event snowfall versus the corresponding state of canopy snow load calculated using the subcanopy lysimeters (SCLs) for each of the 26 snowfall events. The SCLs are denoted by a distinct colour (grey, yellow, and green), correspond to varying canopy coverage (0.73, 0.78, and 0.82, respectively).

Table 2: Meteorology of the 26 snowfall events. Air temperature and wind speed were measured at FT station. Snowfall was measured at PWL station. Interception efficiency is estimated from snowfall and the average throughfall of all three SCLs located within the FT forest plot (all from 15-min. measurements).

Start Date	Air Temperature (°C)			Wind Speed (m/s)			Interception Efficiency (-)			Total Snowfall (mm)
	Min	Mean	Max	Min	Mean	Max	Min	Mean	Max	
2021-12-23	-6.2	-5.3	-4.6	0.6	3.1	4.6	0.7	0.8	1.0	21.7
2022-01-02	-15.9	-10.6	-5.8	0.2	1.9	4.2	0.1	0.7	1.0	32.9
2022-01-17	-14.8	-7.8	-0.8	0.2	1.1	1.8	0.0	0.6	1.0	12.9
2022-01-31	-24.5	-12.1	-6.4	0.1	1.0	1.7	0.2	0.7	1.0	9.1
2022-02-14	-9.9	-9.0	-8.5	0.4	0.8	1.2	0.2	0.5	0.8	1.7
2022-02-19	-4.7	-3.2	-2.5	1.3	2.3	3.6	0.3	0.6	0.9	11.1
2022-03-01	-8.3	-5.4	-1.0	0.1	1.0	3.1	0.4	0.8	1.0	9.9
2022-03-07	-12.5	-8.6	-4.4	0.3	0.8	1.7	0.3	0.7	1.0	9.5
2022-03-14	-2.7	-2.1	-0.8	1.0	1.6	2.9	0.2	0.6	0.9	8.4
2022-03-19	-3.1	-2.8	-2.5	0.0	0.7	1.3	0.3	0.5	0.6	6.6
2022-03-23	-7.9	-5.3	-0.9	0.8	1.2	1.8	0.4	0.6	0.9	1.6
2022-04-04	-3.5	-2.9	-2.1	0.6	1.0	1.9	0.0	0.4	0.6	3.4
2022-04-18	-5.2	-4.0	-2.7	0.4	1.1	1.9	0.1	0.5	0.9	7.4
2022-04-22	-2.8	-1.8	-0.5	0.4	0.8	1.2	0.1	0.5	1.0	9.8
2022-05-09	-4.9	-4.3	-3.2	0.1	0.4	0.9	0.2	0.5	0.9	8.1
2022-05-19	-4.9	-2.1	0.3	0.1	0.4	0.9	0.2	0.6	0.9	7.1
2022-06-13	-1.1	-0.3	0.6	0.1	0.1	0.4	0.0	0.5	0.9	45.3
2022-12-27	-3.0	-2.7	-1.9	0.6	1.1	1.8	0.2	0.5	0.9	4.5
2023-01-27	-11.5	-7.3	-4.5	0.6	0.9	1.2	0.1	0.5	0.8	10.4
2023-02-19	-14.3	-9.5	-6.3	0.2	0.8	1.4	0.2	0.7	1.0	18.1
2023-02-26	-9.2	-8.4	-6.6	0.2	1.0	2.1	0.3	0.5	1.0	5.4
2023-03-13	-8.9	-3.6	-0.1	0.3	1.3	2.2	0.0	0.5	1.0	27.4
2023-03-24	-7.9	-5.7	-3.5	0.1	0.5	1.2	0.1	0.4	0.7	23.8
2023-04-01	-8.9	-7.7	-4.7	0.1	0.6	1.4	0.4	0.6	0.8	11.4
2023-04-10	-1.1	-0.5	0.3	0.1	0.3	1.0	0.2	0.4	0.6	18.0
2023-05-08	0.2	0.6	1.0	0.4	0.6	0.8	0.6	0.6	0.7	3.5

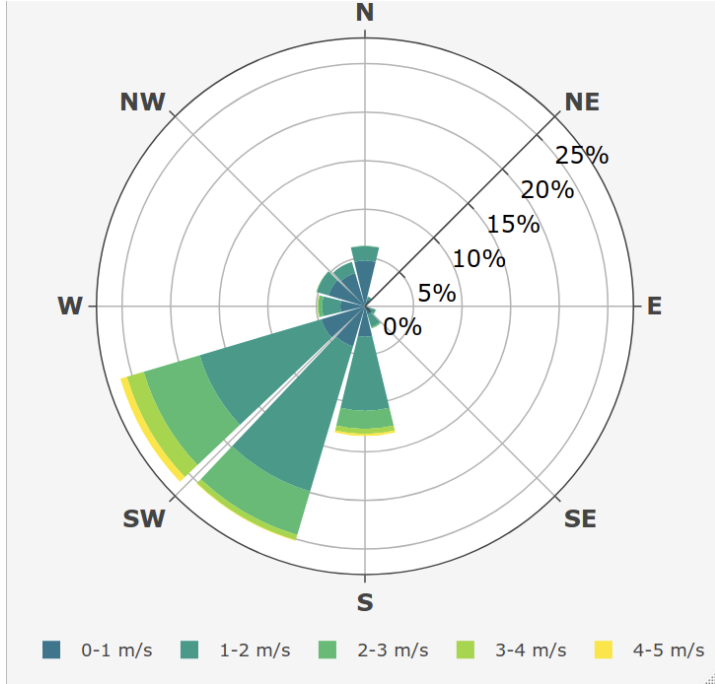


Figure 4: Wind rose showing the frequency of wind speed and direction over the 26 snowfall periods for the ultrasonic anemometer 4.3 m above ground at FT station.

Event average air temperature and interception efficiency were negatively associated for the mixed canopy ($R^2 = 0.1$, $p < 0.05$), but not associated at the closed and sparse canopies (Table 3 & Figure 5). Cumulative event snowfall was not associated with event interception efficiency at any site ($p > 0.05$). Event wind speed was positively associated with interception efficiency for the sparse ($R^2 = 0.1$, $p > 0.05$) and closed ($R^2 = 0.2$, $p < 0.05$) canopies, both with limited canopy openings (Figure 2a,c) towards the prevailing wind direction shown in the wind rose in Figure 4. However, interception efficiency in the mixed canopy, which is partially open towards the prevailing wind direction, was not associated with wind speed ($p > 0.05$).

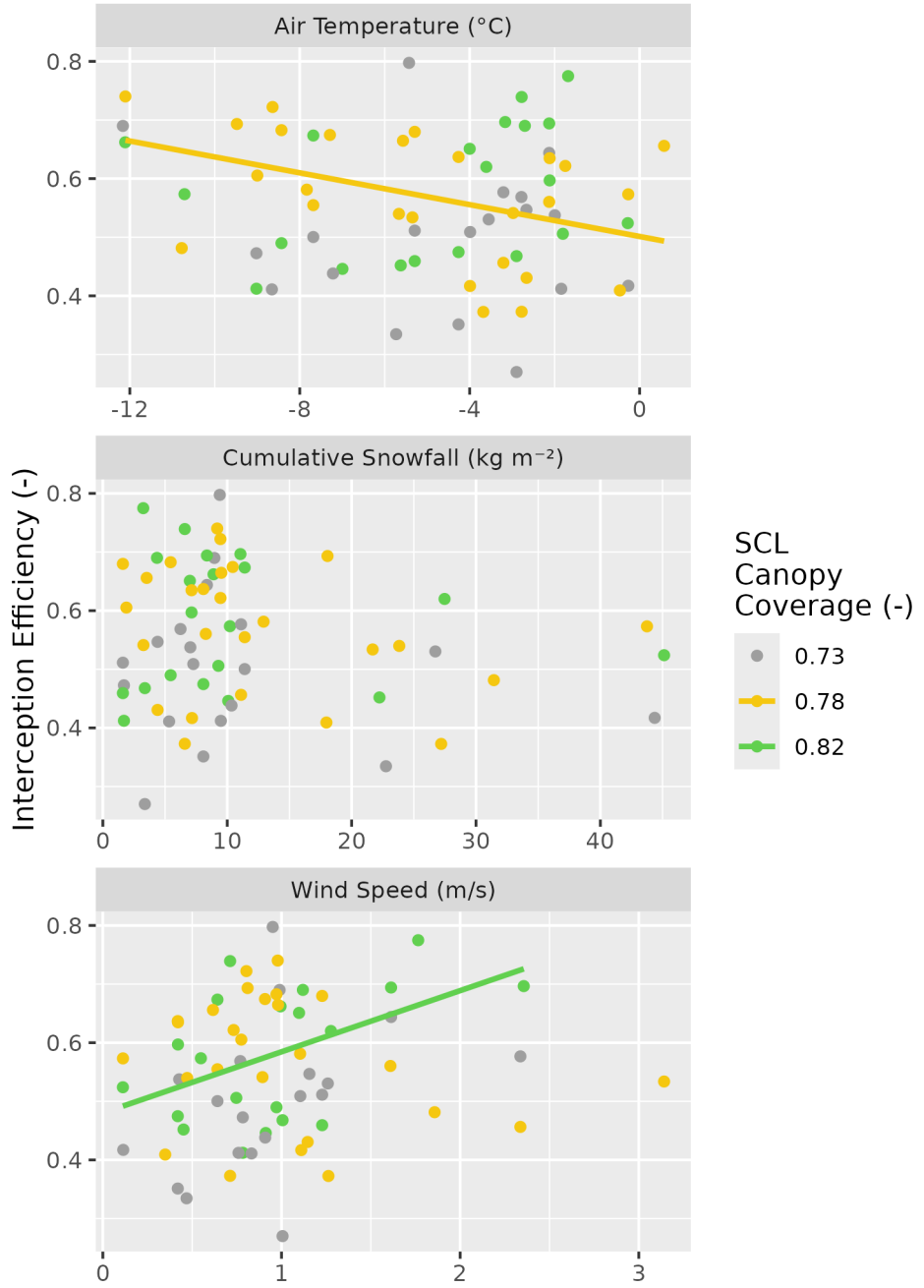


Figure 5: Scatter plots showing the event mean air temperature, mean wind speed, and cumulative snowfall versus the event mean interception efficiency estimated using the SCLs for each of the 26 snowfall events. The colours (grey, yellow, and green), correspond to varying canopy coverage (0.73, 0.78, and 0.82, respectively). A linear regression line fit to the data for significant relationships ($p < 0.05$) is shown by the solid coloured lines. See Table 3 for linear regression statistics.

Table 3: Statistics corresponding to the ordinary least squares linear regression test between independent variables: mean event air temperature, cumulative event snowfall, and mean event wind speed, and the dependent variable mean event interception efficiency. The test was run separately for three levels of canopy coverage (C_c).

SCL					
Dependent Variable	Name	C_c	Adjusted R^2	p-value	n
Air Temperature (°C)	Sparse	0.73	-0.032	0.519	19
Air Temperature (°C)	Mixed	0.78	0.141	0.033	26
Air Temperature (°C)	Closed	0.82	0.008	0.297	20
Cumulative Snowfall (kg m ⁻²)	Sparse	0.73	-0.038	0.568	19
Cumulative Snowfall (kg m ⁻²)	Mixed	0.78	0.030	0.197	26
Cumulative Snowfall (kg m ⁻²)	Closed	0.82	-0.049	0.732	20
Wind Speed (m/s)	Sparse	0.73	0.114	0.087	19
Wind Speed (m/s)	Mixed	0.78	0.010	0.275	26
Wind Speed (m/s)	Closed	0.82	0.192	0.030	20

287 Fifteen-minute interval measurements of interception efficiency and air temperature shown
 288 in Figure 6a were not associated, despite significant relationships for the sparse and mixed
 289 canopies ($R^2 < 0.03$, $p < 0.05$), due to low predictive power (Table 4). The average interception
 290 efficiency across differing bins of air temperature also does not show any systematic trend
 291 (Figure 6a). However, a significantly greater median interception efficiency ($p < 0.05$) was
 292 found for binned measurements with air temperatures below -6 °C compared to those with
 293 warmer air temperatures using non-parametric Wilcoxon signed rank test.

294 Mean wind speed was weakly associated with interception efficiency for the sparse ($R^2 = 0.1$, p
 295 > 0.05) and closed ($R^2 = 0.2$, $p < 0.05$), but not for the mixed canopy ($p > 0.05$) (Table 4). The
 296 binned data show an increasing trend in interception efficiency with increasing wind speed for
 297 the sparse and closed canopies (Figure 6b). A comparison of interception efficiencies binned for
 298 low (< 1 m s⁻¹) and high (> 1 m s⁻¹) wind speeds by the Wilcoxon signed rank test, showed that

²⁹⁹ high wind speeds had significantly higher ($p < 0.05$) median interception efficiencies compared
³⁰⁰ to the low wind speed bins for the closed and sparse canopy. Conversely, the Wilcoxon test
³⁰¹ showed the mixed canopy, which had an opening in the canopy towards the prevailing wind
³⁰² direction (Figure 2b), had significantly higher ($p < 0.05$) median interception efficiencies for
³⁰³ the low wind speed bins.

³⁰⁴ Interception efficiency showed no association ($R^2 < 0.05$, $p > 0.2$) with the canopy load mea-
³⁰⁵ sured at the beginning of the 15-minute intervals (Table 4). The binned data show a small
³⁰⁶ increase in interception efficiency for all three canopies when the snow load is less than 7 kg m^{-2}
³⁰⁷ (Figure 6c). Interception efficiency later declined for snow loads greater than 7 kg m^{-2} for all
³⁰⁸ canopies, though this was inconsistent for the mixed canopy. A significantly greater ($p < 0.05$)
³⁰⁹ median interception efficiency was found for canopy snow loads less than 10 kg m^{-2} than those
³¹⁰ with high initial canopy snow loads ($> 10 \text{ kg m}^{-2}$) using the Wilcoxon rank-test. Additional
³¹¹ statistics from ordinary least squares regression test on the 15-minute interval measurements
³¹² are provided in Table 4.

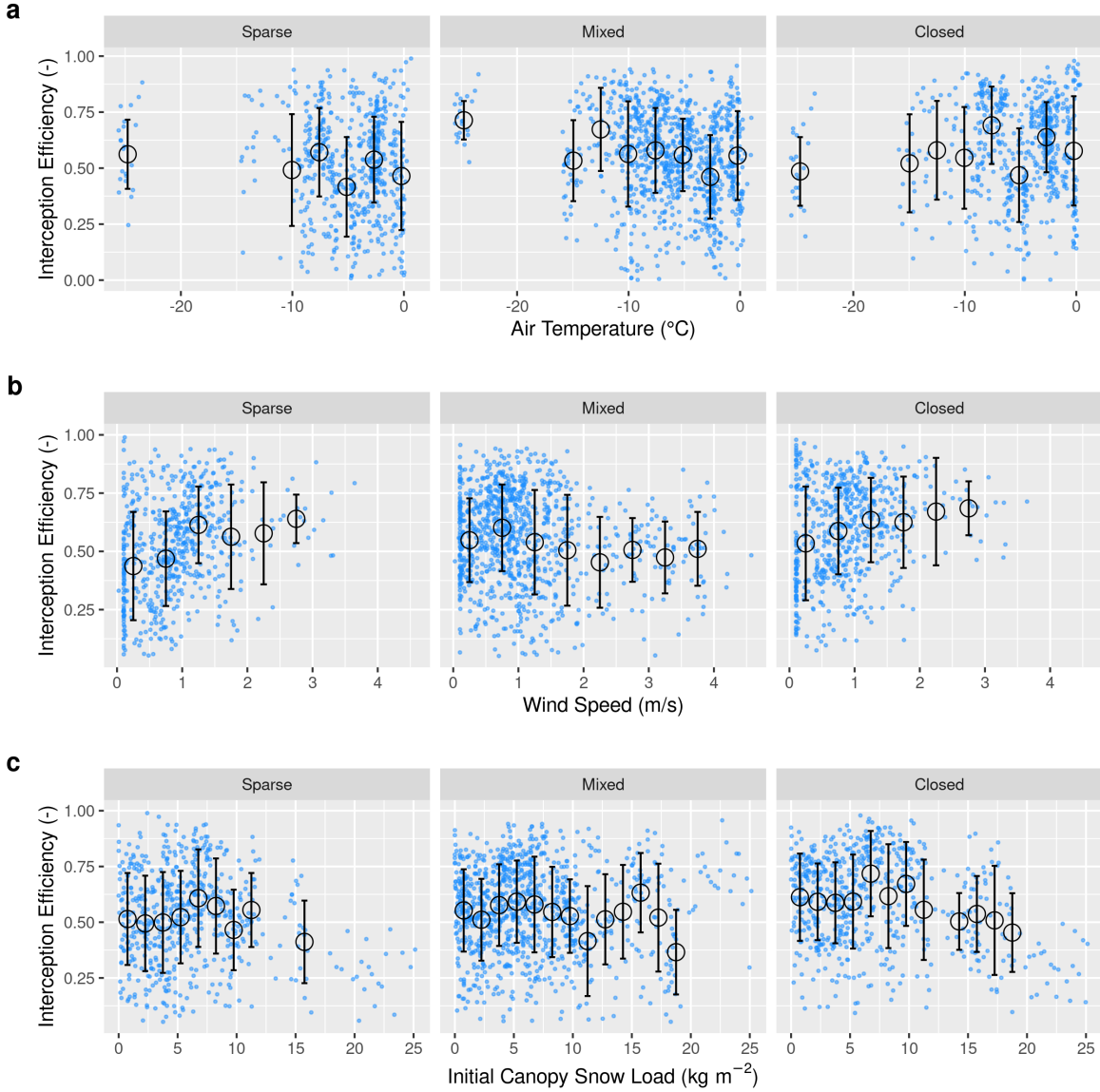


Figure 6: Scatter plots of 15-minute interval measurements (blue dots) and binned data (black open circles with error bars) of mean air temperature, mean wind speed, and initial canopy snow load versus mean snow interception efficiency. Panels show (a) air temperature, (b) wind speed, and (c) initial canopy snow load (the snow load observed at the beginning of the timestep). The black open circles show the mean of each bin and the error bars represent the standard deviations. See Table 4 for linear regression statistics.

Table 4: Statistics corresponding to the ordinary least squares linear regression test between 15-minute interval measurements of independent variables: mean air temperature, mean wind speed, and initial canopy snow load and the dependent variable mean interception efficiency. The test was run separately for three levels of canopy coverage (C_c).

Dependent Variable		SCL	C_c	Adjusted R^2	p-value	n
Air Temperature (°C)	Mixed	0.78	0.032	0.000	985	
Air Temperature (°C)	Closed	0.82	0.004	0.069	618	
Air Temperature (°C)	Sparse	0.73	0.007	0.019	603	
Wind Speed (m/s)	Mixed	0.78	0.017	0.000	985	
Wind Speed (m/s)	Closed	0.82	0.037	0.000	618	
Wind Speed (m/s)	Sparse	0.73	0.089	0.000	603	
Initial Canopy Snow Load (kg m ⁻²)	Mixed	0.78	0.000	0.453	972	
Initial Canopy Snow Load (kg m ⁻²)	Closed	0.82	0.051	0.000	607	
Initial Canopy Snow Load (kg m ⁻²)	Sparse	0.73	0.025	0.000	592	

4.2 The influence of forest structure on snow interception

UAV-lidar measurements of throughfall and canopy structure provide insights on how the forest canopy influenced subcanopy snow accumulation during a wind-driven snowfall event between March 13th and 14th 2023. This event totaled 28.7 kg m⁻² of snowfall at PWL station and was characterized by a transition from low rates of snowfall and air temperatures near 0°C to higher rates of snowfall by late afternoon on March 13th coinciding with air temperatures around -2.5 °C. An average wind speed of 1.3 m s⁻¹ and direction of 188° was observed 4.3 m above the ground at FT Station. Figure 7 shows Cionco's (1965) exponential function for within canopy wind speed was not appropriate for this sparse canopy. The predicted hydrometeor trajectory angles at varying heights, calculated using Equation 4 and the mean observed hydrometeor terminal velocity observed over the event of 0.9 m s⁻¹ are also shown in Figure 7. An average

³²⁴ wind speed of 1.6 m s^{-1} and direction of 188° was calculated by integrating the wind speed
³²⁵ from the surface to the mean canopy height of FT plot. The corresponding trajectory angle
³²⁶ calculated using Equation 4 from this integrated wind speed was 61.5° .

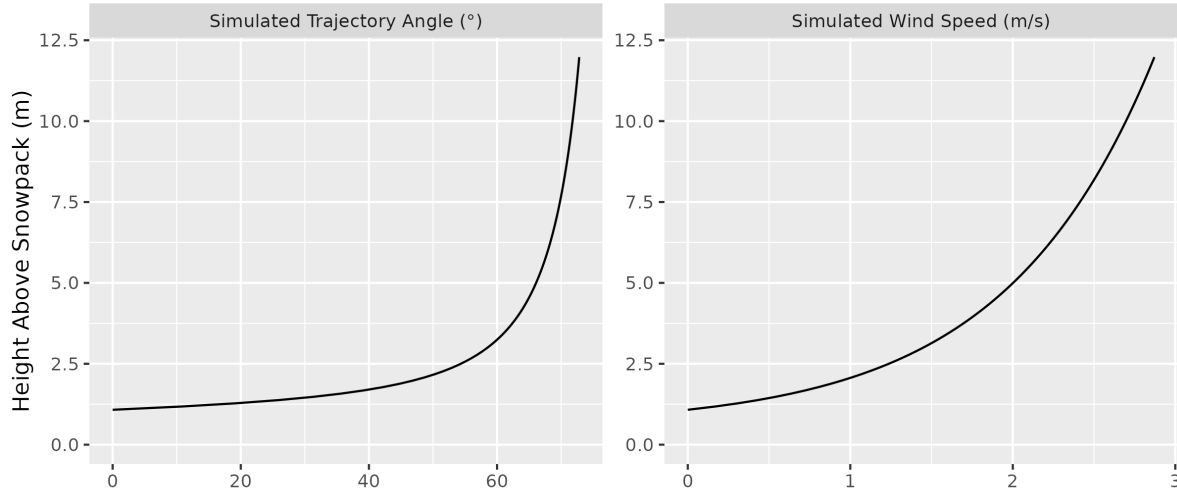


Figure 7: Wind speed profile using roughness length and displacement height parameters derived from anemometers at 2, 3, 4.3, and 13.5 m above ground at FT station over snow free periods and friction velocity estimated over the March 13–14th snowfall event.

³²⁷ Throughfall depth measured by UAV-lidar was close to the 28 in-situ manual measurements
³²⁸ with a mean bias of -0.001 m and RMSE of 0.024 m. More details on the accuracy of UAV-lidar
³²⁹ snowdepth measurements are provided in the supporting information section. Figure 8 shows
³³⁰ the spatial distribution of throughfall and interception efficiency at the PWL and FT forest
³³¹ plots. Reduced throughfall and greater interception efficiency was observed on the north (lee)
³³² side of individual trees, which may be due to non-vertical hydrometeor trajectories caused by
³³³ the steady southerly winds observed over this event. Transparent areas within the forest plots
³³⁴ in Figure 8 represent grid cells that did not have any lidar ground returns (i.e., under dense
³³⁵ canopy proximal to tree trunks) or were masked due to disturbance (i.e., walking paths in
³³⁶ clearings). Visual observations on March 13th and 14th confirmed non-vertical hydrometeor
³³⁷ trajectories and increased canopy snow loads were observed on the windward side of individual

³³⁸ trees. This effect is shown in Figure 8 to be more apparent in the PWL forest plot than the
³³⁹ FT forest plot. This may be attributed to the taller trees and higher canopy coverage of the
³⁴⁰ PWL forest plot compared to the FT forest plot, as for the same trajectory angle a taller tree
³⁴¹ will produce a larger downwind footprint.

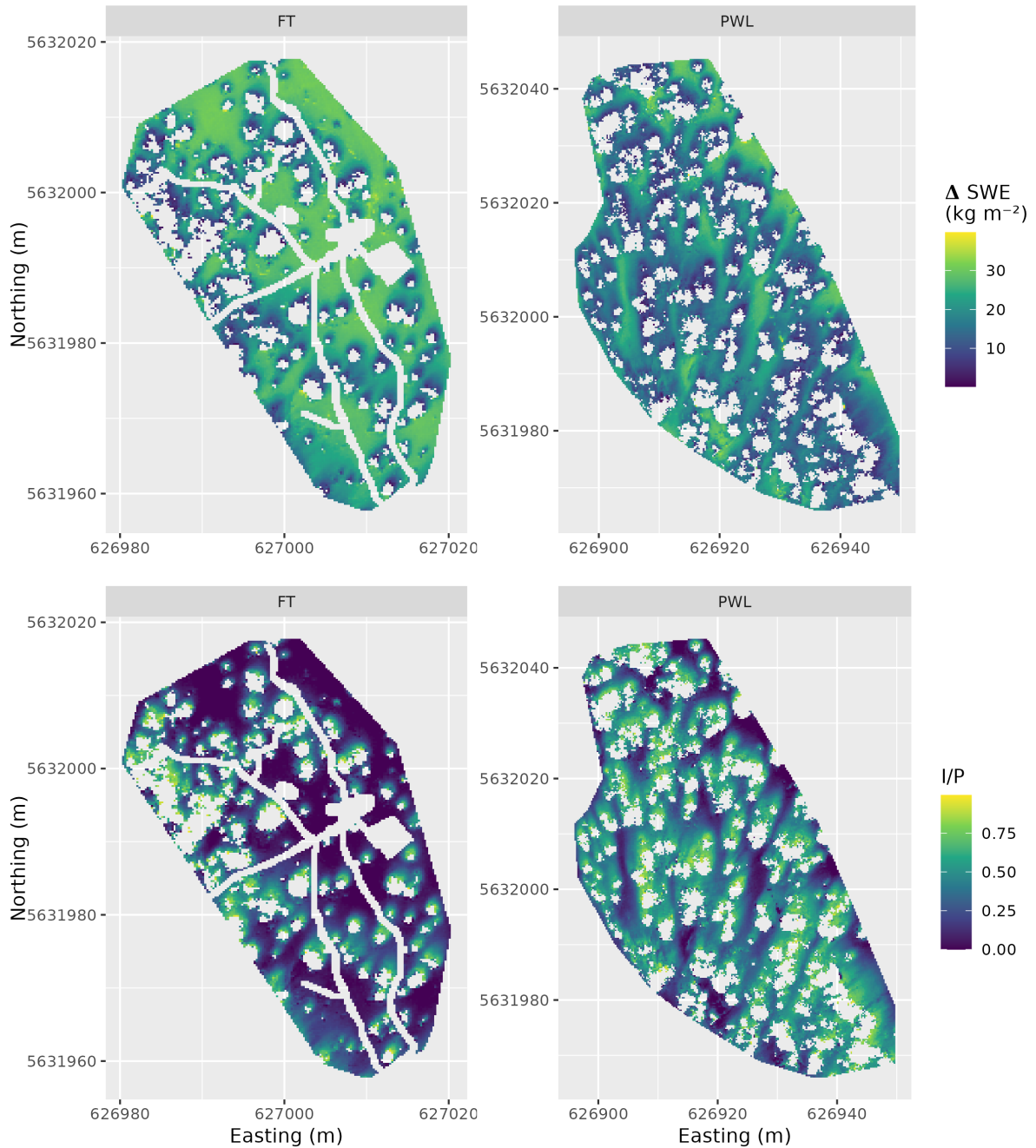


Figure 8: UAV-lidar measurements of the change in snow water equivalent, SWE (kg m^{-2}) and interception efficiency, I/P (-), over the March 13, 2023 24-hour snowfall event for the FT and PWL forest plots at a 0.25 m resolution. See the location of the two forest plots in Figure 1.

Figure 9 shows a strong linear correlation between C_p and interception efficiency towards the southern portion of the hemisphere, aligning with the average event wind direction. For the PWL forest plot, the upper 97.5th percentile of the ρ_p values shown in Figure 9, were found between azimuth angles of 167°–217°. Similarly, for the FT forest plot, the upper 97.5th percentile of ρ_p was found between azimuth angles of 171°–223°. The zenith angle found to have the highest correlation over this azimuth range was 22° ($\rho_p = 0.7$) and 21° ($\rho_p = 0.83$) for PWL and FT respectively. The high correlation coefficients found for non-vertical zenith angles for both PWL and FT are hypothesized to result from non-vertical hydrometeor trajectories.

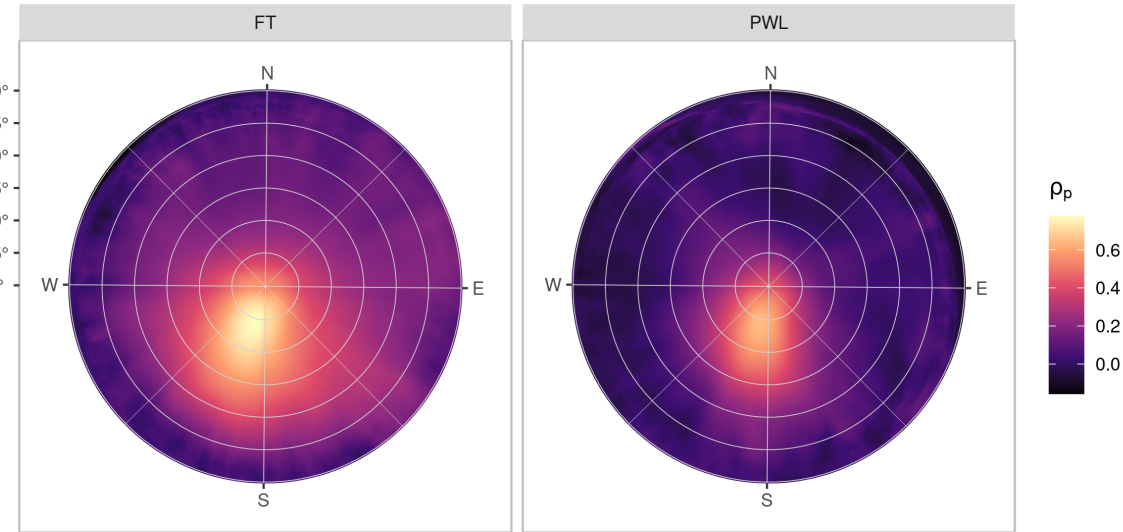


Figure 9: The Pearson Correlation Coefficient between rasters (0.25 m resolution) of interception efficiency and leaf contact area for each grid cell across the study site for each azimuth angles (0°, 1°, ..., 359°) and zenith angles (0°, 1°, ..., 90°) for the FT (left) and PWL (right) forest plots.

The correlation between C_p and interception efficiency, resampled to a 5 m grid resolution, was higher when C_p was adjusted for the observed shift in hydrometeor trajectory (Vector Based), compared to the leaf contact angle measured at a zenith angle of 0° (nadir) (Figure 10). The azimuth and zenith angles observed to have the highest ρ_p in Figure 9 was used to adjust

355 the vector based, C_p in Figure 10. The stronger association for the vector-based calculation
 356 suggests that adjusted C_p is a useful predictor of interception efficiency before ablation. An
 357 ordinary least squares linear regression forced through the origin was fit to the observed data
 358 points using the following equation:

$$\frac{I}{P} = C_p(C_c, \theta_h) \cdot \alpha \quad (9)$$

359 where α is an efficiency constant which determines the fraction of snowflakes that contact the
 360 C_p elements and are stored in the canopy (i.e., intercepted) before canopy snow unloading or
 361 ablation processes begin.

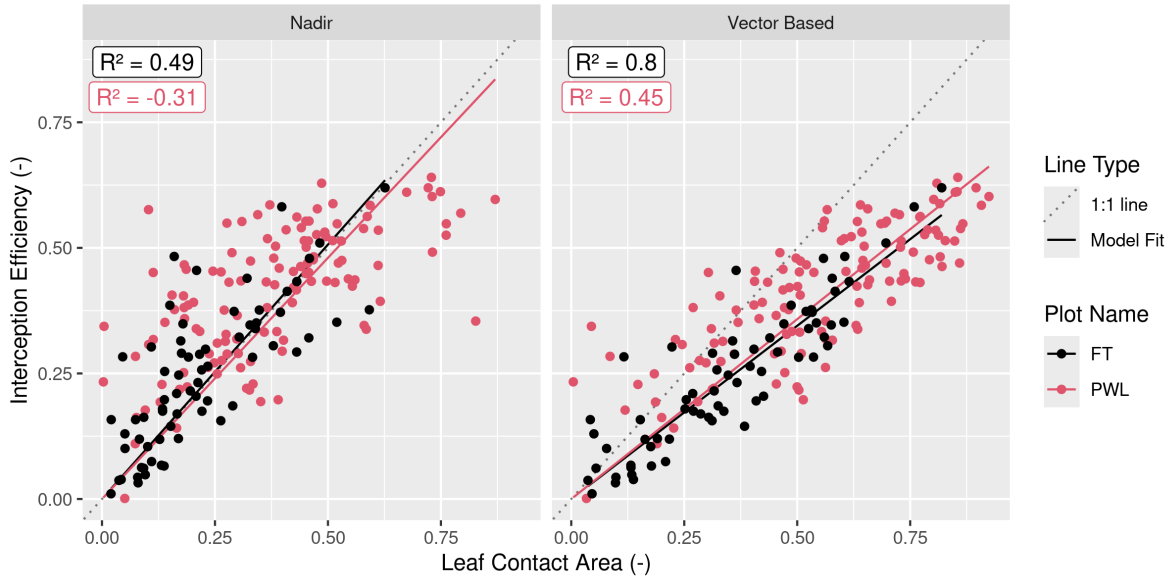


Figure 10: Scatter plots showing the relationship between leaf contact area and interception efficiency rasters resampled to a 5 m grid cell resolution. The left plot (nadir) shows leaf contact area measured from a zenith angle of 0°. The right plot (Vector Based) shows the leaf contact area averaged over rasters with zenith angles (PWL = 22°, FT = 21°) and azimuth angles (PWL = 167°, 178°, ... 217°; FT = 171°, 172°, ... 223°). The solid lines (Model fit) show an ordinary least squares linear regression forced through the origin and fitted to the PWL (red) and FT (black) data and the light grey dotted line shows a 1:1 line. The R^2 values for the four different models are shown in the upper right of each panel calculated following the methods outlined in Kozak & Kozak (1995).

362 For the vector-based model, the relationship between interception efficiency and C_p results in
363 R^2 values of 0.47 and 0.8 for PWL and FT respectively. The increase in interception efficiency
364 with C_p follows a reduced slope compared to the nadir models with α values of 0.71 and 0.68
365 for the PWL and FT vector-based models respectively. The reduced slope for the vector-based
366 models may be due to snowflakes that weaved through and/or bounced off branch elements
367 in addition to UAV-lidar measurement uncertainty which may have been slightly affected by
368 unloading and redistribution. These processes would have reduced the fraction of snowfall
369 that was stored in the canopy. Model error statistics are presented in Table 5 for the nadir
370 and vector-based models and show the vector-based model provided a better prediction of
371 interception efficiency. Some of the scatter observed in the nadir model shown in Figure 10
372 may be explained by grid cells which observed a greater interception efficiency compared to
373 the corresponding C_c value and can be attributed to the inability of C_c to represent the
374 increase in interception observed within canopy gaps in Figure 8. Conversely, grid cells where
375 interception efficiency is less than C_c , may be affected by non-vertical trajectory hydrometeors
376 making their way underneath the canopy as observed by the reduced interception efficiency
377 on the windward edges of individual trees in Figure 8. The latter explanation suggests the
378 non-linear relationship observed for the PWL nadir calculation in Figure 8.

Table 5: Model error statistics provided for predictions of interception efficiency using Equation 9 and for different a values, as shown in the Model Slope column. Statistics are provided for the PWL and FT forest plots, using leaf contact area canopy metrics adjusted to zenith angles of ($0^\circ, 1^\circ, \dots 30^\circ$) and azimuth angles ($170^\circ, 171^\circ, \dots 220^\circ$) and nadir zenith angle of 0° . The Mean bias is the difference in the model and observed values, MAE is the mean of the absolute error, RMS Error is the root mean squared error, R^2 is the coefficient of determination adjusted using Equation 10 in Kozak & Kozak (1995).

Plot	Canopy	Model Slope	Mean Bias	MAE	RMS Error	
Name	Calculation	(-)	(-)	(-)	(-)	R^2
FT	Nadir	0.99	0.022	0.071	0.099	0.51
FT	Vector Based	0.68	0.001	0.047	0.062	0.80
PWL	Nadir	0.95	0.048	0.113	0.146	NA
PWL	Vector Based	0.71	0.019	0.078	0.095	0.47

379 **4.3 The combined influence of trajectory angle and forest structure on
380 interception**

381 Figure 11 shows that C_p , measured from VoxRS prior to snowfall on March 13th, increases
382 substantially with simulated hydrometeor trajectory angle and corresponding simulated wind
383 speed. The standard deviation in VoxRS measured C_p , illustrated by the shaded area in
384 Figure 11, exhibits the broad range in values for individual grid cells across each forest plot.
385 Despite this large scatter, a systematic increase in the mean C_p across both forest plots results
386 from a rise in the number of canopy elements for more horizontal angles, when averaged across
387 each forest plot, over all azimuth angles (see top left panel Figure 11). This results in a large
388 rise in C_p over relatively common estimated wind speeds. For example, with a wind speed
389 of 1 m s^{-1} and estimated trajectory angle of 48° , C_p would increase by 0.31 and 0.28 for the
390 PWL and FT forest plots respectively (Figure 11). This is a fractional increase in the plot C_p
391 from nadir of 0.61 and 0.95 for PWL and FT respectively. The increase in C_p from C_c , with
392 increasing trajectory angle is shown on the bottom row of Figure 11 and exhibits a similar

393 relationship for both forest plots FT and PWL until trajectory angles reach approximately
394 60° . Beyond 60° , the PWL rate of increase slows as the C_p approaches 1.0, while the FT plot,
395 which has lower C_c , continues to rise until around 75° as a C_p of 1.0 is approached. C_p was
396 also quantified across trajectory angles for both PWL and FT on March 14th, post snowfall,
397 and showed a negligible increase in C_p compared to C_p measured on March 13th without snow
398 in the canopy.

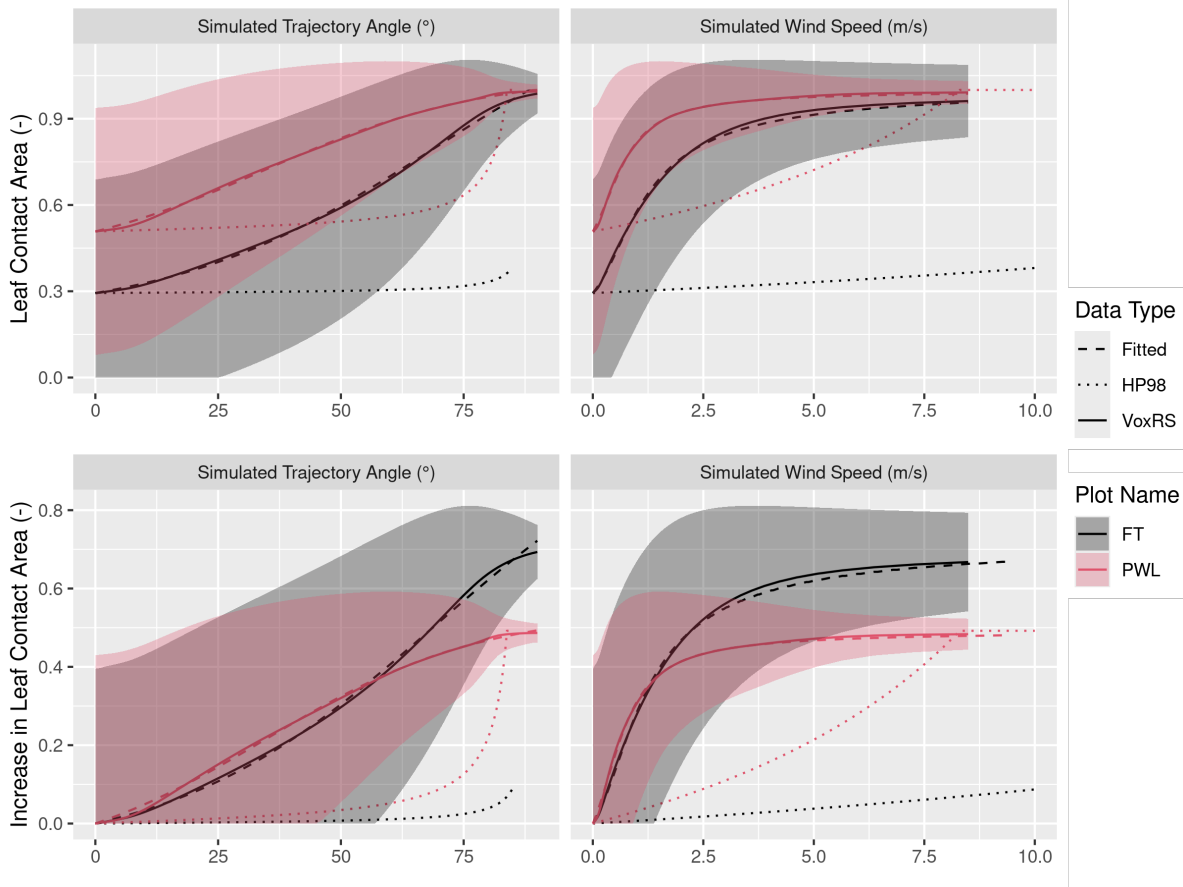


Figure 11: Plots showing the relationship between hydrometeor trajectory angle (left) and wind speed (right) with mean plot-wide snow-leaf contact area, C_p (top row) and the increase in mean plot-wide C_p , i.e., $C_p - C_c$ (bottom row). The hydrometeor trajectory angle is simulated through VoxRS and is measured as degrees from zenith. Simulated wind speed was calculated as a function of hydrometeor trajectory angle by rearranging Equation 4 and an observed event hydrometeor velocity of 0.9 m s⁻¹. The solid lines (VoxRS) represent the mean C_p (top row) or increase in mean C_p (bottom row) for a single zenith angle observed from VoxRS across all grid cells for each forest plot and across all azimuth angles. The shaded area represents 1 standard deviation above and below the observed VoxRS mean. The dashed lines (Fitted) represent predictions from Equation 10 (top) and Equation 11 (bottom). The dotted lines (HP98) represent the predictions from Equation 10 in Hedstrom & Pomeroy (1998). A forested downwind distance of 100 m was assumed for the HP98 calculation.

³⁹⁹ A function is proposed here to calculate plot scale leaf contact area, C_p (-):

$$C_p = C_c + C_{inc}(\theta_h) \quad (10)$$

400 where, C_{inc} is the increase in leaf contact area from C_c which is a function of θ_h . To estimate
 401 C_{inc} a non-linear least squares regression using a logistic function forced through the origin was
 402 fit to the VoxRS measurements at FT and PWL for simulated hydrometeor trajectory angles
 403 (see dashed lines in bottom row of Figure 11). A logistic function was selected to model this
 404 relationship, as its shape reflects the slow increase in observed C_p at near vertical trajectory
 405 angles, followed by a rapid increase to represent increase canopy area in the middle and lower
 406 section of individual trees, and the gradual leveling off as C_p approaches a value of 1.0. The
 407 logistic function used to predict C_{inc} as a function of θ_h is:

$$C_{inc} = \left(\frac{C_{inc}^{max}}{1 + e^{\left(\frac{\theta_0 - \theta_h}{k}\right)}} - \frac{C_{inc}^{max}}{1 + e^{\left(\frac{\theta_0}{k}\right)}} \right) \quad (11)$$

408 where C_{inc}^{max} is the maximum value of C_{inc} , θ_0 is the x-value of the sigmoid midpoint and k is the
 409 logistic growth rate or steepness of the curve. The coefficients resulting from the non-linear
 410 least squares regression fit of Equation 11 to the VoxRS dataset are presented in Table 6.
 411 Simulated C_p using Equation 10 is shown in the dashed lines in the top row of Figure 11
 412 and follows the VoxRS-measured mean C_p closely. Model error statistics shown in Table 7
 413 demonstrate that Equation 11 performed well, with a mean bias and RMSE of 0.001 (-) and
 414 0.0054 (-) respectively for PWL, and -0.0004 (-) and 0.0079 (-) for FT. In contrast, Table 7
 415 reveals that the Hedstrom & Pomeroy (1998) method produced significantly less accurate
 416 estimates of C_p , with a mean bias and RMSE of -0.201 (-) and 0.233 (-) respectively for PWL,
 417 and -0.260 (-) and 0.324 (-) for FT.

Table 6: Coefficients derived from the non-linear least squares regression fit of Equation 11 to the VoxRS dataset.

Plot Names	C_{inc}^{max}	θ_0	k
PWL	0.66	34.58	22.14
FT	1.18	69.13	26.98

Table 7: Model error statistics calculated for the prediction of leaf contact area from trajectory angle using Equation 11 (nls) and Equation 10 from Hedstrom & Pomeroy (1998) for the PWL and FT forest plots. Mean bias is the difference in the model and observed values, MAE is the mean of the absolute error, RMS Error is the root mean squared error and R^2 is the coefficient of determination. The units for all metrics are dimensionless. A forested downwind distance of 100 m was used for the HP98 calculation.

Model	Plot Name	Mean Bias (-)	MAE (-)	RMS Error (-)	R^2
HP98	FT	-0.26	0.26	0.32	0.72
HP98	PWL	-0.20	0.20	0.23	0.44
nls	FT	0.00	0.01	0.01	1.00
nls	PWL	0.00	0.00	0.01	1.00

418 4.4 Throughfall model performance

419 The performance of Equations 9, 10, and 11 in estimating event throughfall was assessed
 420 against UAV-lidar measurements of throughfall for the March 13–14th snowfall event at the
 421 plot scale for both FT and PWL. Required values for the model included the event mean
 422 hydrometeor terminal velocity and event total snowfall which were measured at PWL station,
 423 and wind speed was taken as one-third the mean canopy height using the wind speed profile in
 424 Figure 7. Additional model inputs include the mean C_c for each plot which was measured from
 425 the VoxRS dataset. An α value of 0.836 (-) was found through calibration which provided the

⁴²⁶ best fit between observed and simulated interception efficiency at the plot scale for both FT
⁴²⁷ and PWL.

⁴²⁸ Figure 12 shows the vector-based model, computed using Equation 9 with C_p adjusted for
⁴²⁹ estimated hydrometeor trajectory angle, closely matches UAV-lidar measurements of through-
⁴³⁰ fall. Observed and modelled values of interception efficiency and ΔSWE_{tf} are presented in
⁴³¹ Table 8 along with corresponding error statistics. Modelled throughfall from the vector-based
⁴³² model was 17 kg m^{-2} compared to the measured throughfall of 16.6 kg m^{-2} for PWL. For FT,
⁴³³ the modelled throughfall was 21.8 kg m^{-2} , while the measured values were 22.1 kg m^{-2} . The
⁴³⁴ vector-based model shows a lower mean bias of -0.3 kg m^{-2} for PWL and a negative bias of
⁴³⁵ 0.3 kg m^{-2} for FT, compared to the larger mean bias of -1.6 kg m^{-2} for PWL and -0.8 kg m^{-2}
⁴³⁶ for FT with the nadir-model (calculated using C_c in place of C_p). This resulted in a large
⁴³⁷ reduction in the percent error in predicted throughfall, from -9.4% with the nadir-model to
⁴³⁸ -1.8% with the vector-based model for PWL. A smaller improvement was observed for FT,
⁴³⁹ with the percent error in predicted throughfall declining from -3.6% with the nadir-model to
⁴⁴⁰ -1.4% with the vector-based model.

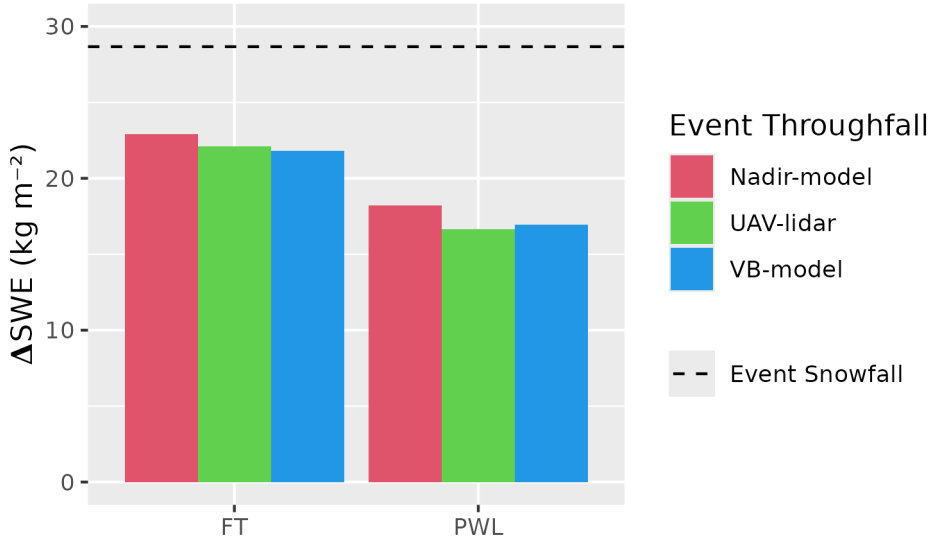


Figure 12: Bar chart comparing the observed and modelled mean change in throughfall (SWE, kg m^{-2}) over the March 13-14 snowfall event averaged over forest plots FT and PWL. The ‘Nadir-model’ used Equation 9 not adjusted for trajectory angle (i.e., C_c) and the Vector-based ‘VB-model’ which uses Equation 9 with C_p adjusted for trajectory angle. ‘UAV-lidar’ corresponds to throughfall calculated using Equation 6 incorporating UAV-lidar snow depth and snow density from in-situ snow pits. The black horizontal dashed line shows the accumulated SWE (kg m^{-2}) over the snowfall event to the PWL station open clearing.

Table 8: Model error statistics for model estimates of snow interception efficiency (I/P) and throughfall (TF) compared to measurements of I/P and TF using UAV-lidar averaged over the FT and PWL forest plots. Units for I/P are (-) and TF are (kg m^{-2}). The vector-based model utilized Equation 9 with C_p adjusted for trajectory angle. The nadir model also utilized Equation 9 but was not adjusted for trajectory angle and thus C_c was used instead of C_p . The ‘Obs. Value’ column contains measurements from UAV-lidar while the ‘Mod. Value’ column contains the modelled values. The mean bias was calculated as observed minus modelled and percent error is the percent error between predicted and observed values.

Plot	Type	Model	Value	Units	Obs.	Mod.	Mean	
		Name			Value	Value	Bias	Perc. Error
FT	VB-model	I/P	-	-	0.23	0.24	-0.01	-4.67
FT	Nadir-model	I/P	-	-	0.23	0.20	0.03	12.10
FT	VB-model	TF	kg m^{-2}	kg m^{-2}	22.12	21.82	0.31	1.38
FT	Nadir-model	TF	kg m^{-2}	kg m^{-2}	22.12	22.91	-0.79	-3.58
PWL	VB-model	I/P	-	-	0.42	0.41	0.01	2.54
PWL	Nadir-model	I/P	-	-	0.42	0.37	0.05	12.95
PWL	VB-model	TF	kg m^{-2}	kg m^{-2}	16.64	16.95	-0.31	-1.84
PWL	Nadir-model	TF	kg m^{-2}	kg m^{-2}	16.64	18.20	-1.56	-9.35

441 5 Discussion

442 The point scale observations presented in Figure 6 show air temperature had little influence
 443 on interception efficiency. This differs from existing studies which suggested either a positive
 444 (Storck et al., 2002) or negative (Hedstrom & Pomeroy, 1998) relationship. A weak relation-
 445 ship, that leaves 80–90% of variance unexplained, was observed between initial interception

⁴⁴⁶ efficiency (before unloading) with increasing wind speed at two locations which were sheltered
⁴⁴⁷ from the predominant wind direction (Figure 6b). This is attributed to an associated increase
⁴⁴⁸ in C_p due to non-vertical hydrometeor trajectories. These results are consistent with observa-
⁴⁴⁹ tions by Schmidt & Troendle (1989) who observed a slight increase in snowfall interception
⁴⁵⁰ with increasing wind speeds up to 6 m s^{-1} and studies of rainfall interception by Herwitz &
⁴⁵¹ Slye (1995) and Van Stan et al. (2011).

⁴⁵² Compared to the influence of wind speed, interception efficiency showed a smaller sensitivity
⁴⁵³ to canopy snow load at the point scale (Figure 5). The slight increase in interception efficiency
⁴⁵⁴ for smaller canopy snow loads and decline for larger canopy snow loads is attributed to the
⁴⁵⁵ influence of canopy snow load on C_p (Figure 6c). While small, this effect is consistent with
⁴⁵⁶ the theory proposed by Satterlund & Haupt (1967) that interception efficiency increases as
⁴⁵⁷ the canopy fills with snow bridging gaps in the canopy increasing, while later declining due to
⁴⁵⁸ branch bending and decreased canopy coverage. However, the observations shown in Figure 6
⁴⁵⁹ and Figure 3, which minimized ablation processes, differ from those reported by Satterlund
⁴⁶⁰ & Haupt (1967), Schmidt & Pomeroy (1990), and Moeser et al. (2015), as canopy snow load
⁴⁶¹ increased linearly with snowfalls up to 45 kg m^{-2} without approaching a maximum canopy snow
⁴⁶² load. The strong decline in interception efficiency with increasing event snowfall in Satterlund
⁴⁶³ & Haupt (1967) and Schmidt & Pomeroy (1990) may have resulted from higher unloading rates
⁴⁶⁴ as branches bent under heavy snow loads, hence mixing ablation and interception processes to
⁴⁶⁵ varying degrees. In contrast, other studies (Calder, 1990; Lundquist et al., 2021; Watanabe &
⁴⁶⁶ Ozeki, 1964) align with the observations in Figure 6 and Figure 3, showing little evidence of
⁴⁶⁷ a reduced interception efficiency with increasing snowfall. The low sensitivity of interception
⁴⁶⁸ efficiency with canopy snow load found in this study and others may be attributed to several
⁴⁶⁹ factors: a reduced inclusion of ablation processes in the interception efficiency measurements,
⁴⁷⁰ limited influence of canopy snow load on C_p at this study site, and/or the compensatory effects
⁴⁷¹ outlined by Satterlund & Haupt (1967).

⁴⁷² Staines & Pomeroy (2023) showed a slight increase in VoxRS measured C_p between snow-off
⁴⁷³ and snow-on conditions. However, the increase in C_p resulting from snow load in Staines

& Pomeroy (2023) was small compared to the substantial rise in C_p due to trajectory angle presented in their study and as shown in Figure 11. Both findings from Staines & Pomeroy (2023) corroborate the results reported in this study. Further evidence in support of the relatively small influence of canopy snow load on C_p , is provided by Lundquist et al. (2021) who reported improved simulation of subcanopy snow accumulation without the use of a maximum canopy snow load, when linked with a comprehensive canopy snow ablation routine. Lehtonen et al. (2016) also note that in northern Finland heavy canopy snow loads have been observed to continue increasing until stem breakage, under conditions favourable for the formation of significant rime-ice accretion and limited ablation, thus reducing C_p . Models are available to predict the accretion of ice on tree canopies (e.g., Nock et al., 2016) however, further research is required to understand the canopy snow load required to cause stem breakage across different tree species and canopy loads.

These findings on the limited influence of air temperature and canopy snow load on initial interception challenge the theoretical basis of many existing snow interception parameterizations (Hedstrom & Pomeroy, 1998; Moeser et al., 2015; Satterlund & Haupt, 1967; Storck et al., 2002). To address this a new snow interception parameterization, Equation 9, is presented which calculates interception efficiency as a function of C_p and α . This new parameterization allows for canopy snow loading processes to be isolated from canopy snow ablation processes and is consistent with current rainfall interception theory (Valante et al., 1997). Equation 9 differs only slightly from the original Hedstrom & Pomeroy (1998) parameterization (see Equation 6 in Hedstrom & Pomeroy (1998)), in that it does not calculate interception efficiency as a function of canopy snow load and from the Storck et al. (2002) parameterization who proposed interception efficiency to be constant over time and space. The theoretical basis of the α parameter in Equation 9 is that the association between C_p and interception efficiency, as shown in Figure 10, unlike existing rainfall parameterizations (Valante et al., 1997) does not follow a 1:1 line, as falling snow hydrometeors may bounce off the canopy elements. Further research is needed to explore how processes such as the increased cohesion and adhesion of snowfall to the canopy at warm temperatures, as observed by Kobayashi (1987), Pfister &

502 Schneebeli (1999), Storck et al. (2002), as well as hydrometeor velocity, particle size, and
503 shape suggested by (Katsushima et al., 2023), may influence the α parameter, although these
504 effects were not observed in this study.

505 Measurements of interception efficiency and canopy structure, as shown in Figure 8, align with
506 the theory proposed by Hedstrom & Pomeroy (1998) which suggests reduced throughfall on
507 the lee side of individual trees. However, an existing method proposed in Hedstrom & Pomeroy
508 (1998) to scale canopy coverage with wind speed failed to reproduce the observations presented
509 in Figure 11. A new method is proposed which uses a logistic function to calculate plot-wide
510 C_{inc} as a function of θ_h and C_c . Significant scatter in VoxRS measured C_p across the two
511 forest plots, illustrated by the high standard deviation in Figure 11, resulted from directional
512 (azimuth) and spatial differences in canopy structure. This large scatter suggests the observed
513 relationships in Figure 11 are only applicable at the forest stand scale where the sub-metre
514 variability in C_p averages out. At the point scale, the mixed canopy SCL which is open to the
515 prevailing wind direction (Figure 2), and did not follow this relationship and led to an increase
516 in throughfall with increasing wind speed (Figure 5 & Figure 6). However, Figure 11 shows
517 that at the plot scale, C_p rises with increasing θ_h , as there is a greater number of grid cells
518 which have more closed canopy at more horizontal angles. Thus at the plot scale, Equation 11,
519 which uses trajectory angle alone, was shown to successfully determine C_{inc} and thus C_p for
520 the discontinuous canopies of both the FT and PWL forest plots. However, Equation 11 would
521 not be applicable to areas that have large continuous gap fractions (e.g., large forested clear
522 cuts) that are many times wider than the mean canopy height. Further work is required to
523 refine the relationship proposed in Equation 11 across a range of tree species and densities.
524 Backflows and large eddies that occur within the canopy may also contribute to very mixed
525 responses (Staines & Pomeroy, 2023).

526 It was found that the mean hydrometeor trajectory angle over a snowfall event, required for
527 Equation 11, could be predicted by using the observed hydrometeor fall velocity and a mean
528 horizontal wind speed selected at one-third of the canopy height above the ground. A wind
529 speed at one-third the mean canopy height is hypothesized to be important for canopy snow

530 accumulation as a large fraction of the horizontal cross-sectional area is at this height for most
531 needleleaf canopies. Katsushima et al. (2023), also proposed the wind speed at one-third the
532 canopy height for modelling unloading of canopy snow as it corresponds to the centre of gravity
533 when the horizontal projection of the canopy is assumed to be a triangle. However, there is
534 uncertainty in the transferability of the canopy height observed here to other environments
535 due to differing tree structures and tree species. This may include forests with a larger trunk
536 space or have more of their canopy contact area at higher heights above the ground (i.e., some
537 deciduous canopies). Moreover, Equation 4 assumes a linear hydrometeor trajectory, and does
538 not consider non-linear patterns such as wind flow directions around tree elements, turbulent
539 flow, or differences in wind speed with height.

540 Although the improvement in performance of the vector-based model over the nadir model was
541 relatively small, the vector-based model is preferred due to its overall lower error compared
542 to the UAV-lidar measurements and better representation of physical processes. While the
543 vector-based model acts to increase interception efficiency with wind speed, several studies
544 have shown that canopy snow ablation increases as a result of wind induced unloading (Bartlett
545 & Verseghy, 2015; Betts & Ball, 1997; Lumbrazo et al., 2022; Roesch et al., 2001; Wheeler,
546 1987). Thus, representing both the increase in initial interception due to inclined hydrometeor
547 trajectory angles and the subsequent increase in canopy snow unloading will be important in
548 subcanopy snow accumulation models.

549 **6 Conclusions**

550 New observations of initial snow interception, collected over a wide range of meteorological
551 conditions and canopy structures suggest forest structure is the primary factor governing
552 subcanopy snow accumulation. At the point scale, high-temporal resolution measurements
553 revealed no evidence of a maximum canopy snow load, even for event snowfalls up to 45 kg
554 m⁻², nor was there any indication of air temperature influencing the cohesion and adhesion of
555 snowfall to the canopy or branch bending reducing canopy coverage. Instead, wind speed was

556 found to influence interception efficiency by changing the hydrometeor trajectory angle, which
557 can lead to a substantial increase in snow-leaf contact area.

558 At the forest plot scale, UAV-lidar measurements of throughfall collected over a wind-driven
559 snowfall event confirmed the results observed at the point-scale and showed leaf contact area
560 was the main factor governing the interception efficiency at a particular site. The leaf contact
561 area, which accounts for the change in canopy structure with trajectory angle, proved to be
562 a better predictor of interception efficiency compared to nadir-calculated canopy coverage.
563 When averaged across each forest plot, leaf contact area was shown to be highly sensitive to
564 hydrometeor trajectory angle, increasing by 61–95% for trajectory angles associated with a
565 1 m s⁻¹ wind speed. An existing theoretical relationship failed to adequately represent the
566 VoxRS-measured increase in leaf contact area with simulated trajectory angles. As a result, a
567 new relationship is proposed, which demonstrated good performance at this study site.

568 The weak association between air temperature and canopy snow load with interception effi-
569 ciency, as presented here and in other recent studies, coupled with the influence of wind speed
570 on leaf contact area, highlights the need for a new snow interception parameterization. A new
571 parameterization is proposed that calculates initial interception as a function of snowfall and
572 leaf contact area. This parameterization is consistent with many rainfall interception stud-
573 ies, which also separate canopy loading and ablation processes, and calculate interception as
574 a function of canopy coverage. Additionally, a second equation is proposed to estimate leaf
575 contact area as a function of hydrometeor trajectory angle and nadir canopy coverage. This
576 updated snow interception parameterization showed good performance in the subalpine forest
577 in this study, but further validation should be conducted in a range of climates, forest species,
578 and canopy structures.

579 **7 Acknowledgments**

580 We wish to acknowledge financial support from the University of Saskatchewan Dean's Schol-
581 arship, Natural Sciences and Engineering Research Council of Canada, Global Water Futures

582 Programme, Environment and Climate Change Canada, Alberta Innovates, Canada Founda-
583 tion for Innovation, and the Canada Research Chairs Programme. We thank Madison Harasyn,
584 Hannah Koslowsky, Kieran Lehan, Lindsey Langs and Fortress Mountain Resort for their help
585 in the field. Jacob Staines, Madison Harasyn, Alistair Wallace, and Rob White contributed
586 to developing the UAV-lidar processing workflow.

587 **8 Data Availability**

588 The data that support the findings in this study are available at <https://doi.org/10.5281/zenodo.14018893>.

589 **References**

- 590 Bartlett, P. A., & Verseghy, D. L. (2015). Modified treatment of intercepted snow improves
591 the simulated forest albedo in the Canadian Land Surface Scheme. *Hydrological Processes*,
592 29(14), 3208–3226. <https://doi.org/10.1002/HYP.10431>
- 593 BayesMap Solutions. (2024). *BayesStripAlign*. <https://bayesmap.com/products/bayesstripalign/>
- 595 Betts, A. K., & Ball, J. H. (1997). Albedo over the boreal forest. *Journal of Geophysical*
596 *Research: Atmospheres*, 102(D24), 28901–28909. [https://doi.org/https://doi.org/10.1029/96JD03876](https://doi.org/10.1029/96JD03876)
- 598 Calder, I. R. (1990). *Evaporation in the uplands* (p. 148). Wiley.
- 599 Cebulski, A., & Pomeroy, J. W. (2024). The theoretical underpinnings of snow interception
600 and ablation parameterizations. *Wiley Interdisciplinary Reviews: Water, In Review*.
- 601 Chianucci, F., & Macek, M. (2023). hemispheR: an R package for fisheye canopy image
602 analysis. *Agricultural and Forest Meteorology*. <https://doi.org/10.1016/j.agrformet.2023.109470>
- 604 Cionco, R. M. (1965). A Mathematical Model for Air Flow in a Vegetative Canopy. *Journal of*
605 *Applied Meteorology* (1962), 4(4), 517–522. [https://doi.org/https://doi.org/10.1175/1520-0450\(1965\)004%3C0517:AMMFAF%3E2.0.CO;2](https://doi.org/https://doi.org/10.1175/1520-0450(1965)004%3C0517:AMMFAF%3E2.0.CO;2)
- 607 Clark, M. P., Wood, A., Nijssen, B., Bennett, A., Knoben, W., & Lumbrazo, C. (2020).
608 *SUMMA v3.0.3*. Zenodo. <https://doi.org/10.5281/zenodo.4558054>
- 609 Ellis, C. R., Pomeroy, J. W., & Link, T. E. (2013). Modeling increases in snowmelt yield and
610 desynchronization resulting from forest gap-thinning treatments in a northern mountain
611 headwater basin. *Water Resources Research*, 49(2), 936–949. <https://doi.org/10.1002/wrcr.20089>
- 613 Essery, R., Pomeroy, J. W., Parviainen, J., & Storck, P. (2003). Sublimation of snow from
614 coniferous forests in a climate model. *Journal of Climate*, 16(11), 1855–1864. [https://doi.org/10.1175/1520-0442\(2003\)016%3C1855:SOSFCF%3E2.0.CO;2](https://doi.org/10.1175/1520-0442(2003)016%3C1855:SOSFCF%3E2.0.CO;2)
- 616 Fryer, B. Y. G. I., Johnson, E. A., Fryer, G. I., & Johnson, E. A. (1988). Reconstructing

- 617 Fire Behaviour and Effects in a Subalpine Forest. *The Journal of Applied Ecology*, 25(3),
618 1063–1072. [https://doi.org/https://doi.org/10.2307/2403766](https://doi.org/10.2307/2403766)
- 619 Gelfan, A. N., Pomeroy, J. W., & Kuchment, L. S. (2004). Modeling forest cover influences on
620 snow accumulation, sublimation, and melt. *Journal of Hydrometeorology*, 5(5), 785–803.
621 [https://doi.org/10.1175/1525-7541\(2004\)005%3C0785:MFCIOS%3E2.0.CO;2](https://doi.org/10.1175/1525-7541(2004)005%3C0785:MFCIOS%3E2.0.CO;2)
- 622 Golding, D. L., & Swanson, R. H. (1978). Snow accumulation and melt in small forest openings
623 in Alberta. *Canadian Journal of Forest Research*, 8(4), 380–388. <https://doi.org/https://doi.org/10.1139/x78-057>
- 625 Harder, P., & Pomeroy, J. W. (2013). Estimating precipitation phase using a psychrometric
626 energy balance method. *Hydrological Processes*, 27(13), 1901–1914. <https://doi.org/https://doi.org/10.1002/hyp.9799>
- 628 Harder, P., Pomeroy, J. W., & Helgason, W. D. (2020). Improving sub-canopy snow depth
629 mapping with unmanned aerial vehicles: Lidar versus structure-from-motion techniques.
630 *Cryosphere*, 14(6), 1919–1935. <https://doi.org/10.5194/tc-14-1919-2020>
- 631 Harpold, A. A., Krogh, S. A., Kohler, M., Eckberg, D., Greenberg, J., Sterle, G., & Broxton,
632 P. D. (2020). Increasing the efficacy of forest thinning for snow using high-resolution
633 modeling: A proof of concept in the Lake Tahoe Basin, California, USA. *Ecohydrology*,
634 13(4). <https://doi.org/10.1002/eco.2203>
- 635 Hedstrom, N. R., & Pomeroy, J. W. (1998). Measurements and modelling of snow interception
636 in the boreal forest. *Hydrological Processes*, 12(10-11), 1611–1625. [https://doi.org/10.1002/\(SICI\)1099-1085\(199808/09\)12:10/11%3C1611::AID-HYP684%3E3.0.CO;2-4](https://doi.org/10.1002/(SICI)1099-1085(199808/09)12:10/11%3C1611::AID-HYP684%3E3.0.CO;2-4)
- 638 Herwitz, S. R., & Slye, R. E. (1995). Three-dimensional modeling of canopy tree interception
639 of wind-driven rainfall. *Journal of Hydrology*, 168(1-4), 205–226. [https://doi.org/10.1016/0022-1694\(94\)02643-P](https://doi.org/10.1016/0022-1694(94)02643-P)
- 641 Hijmans, R. J. (2024). *terra: Spatial Data Analysis*. <https://cran.r-project.org/package=terra>
- 642 Katsushima, T., Kato, A., Aiura, H., Nanko, K., Suzuki, S., Takeuchi, Y., & Murakami, S.
643 (2023). Modelling of snow interception on a Japanese cedar canopy based on weighing
644 tree experiment in a warm winter region. *Hydrological Processes*, 37(6), 1–16. <https://doi.org/10.1002/hyp.14922>

- 646 Kim, E., Gatebe, C., Hall, D., Newlin, J., Misakonis, A., Elder, K., Marshall, H. P., Hiemstra, C., Brucker, L., De Marco, E., Crawford, C., Kang, D. H., & Entin, J. (2017).
647 NASA's snowex campaign: Observing seasonal snow in a forested environment. *2017*
648 *IEEE International Geoscience and Remote Sensing Symposium (IGARSS)*, 1388–1390.
649
650 <https://doi.org/10.1109/IGARSS.2017.8127222>
- 651 Kobayashi, D. (1987). Snow accumulation on a narrow board. *Cold Regions Science and*
652 *Technology*, 13(3), 239–245. [https://doi.org/https://doi.org/10.1016/0165-232X\(87\)90005-X](https://doi.org/https://doi.org/10.1016/0165-232X(87)90005-X)
- 653
654 Kozak, A., & Kozak, R. A. (1995). Notes on regression through the origin. *Forestry Chronicle*,
655 71(3), 326–330. <https://doi.org/https://doi.org/10.5558/tfc71326-3>
- 656 Langs, L. E., Petrone, R. M., & Pomeroy, J. W. (2020). A $\delta^{18}\text{O}$ and $\delta^2\text{H}$ stable water
657 isotope analysis of subalpine forest water sources under seasonal and hydrological stress
658 in the Canadian Rocky Mountains. *Hydrological Processes*, 34(26), 5642–5658. <https://doi.org/10.1002/hyp.13986>
- 659
660 LAStools. (2024). *Efficient LiDAR Processing Software (version 240220, academic)*. <http://rapidlasso.com/LAStools>
- 661
662 Lehtonen, I., Kämärainen, M., Gregow, H., Venäläinen, A., & Peltola, H. (2016). Heavy snow
663 loads in Finnish forests respond regionally asymmetrically to projected climate change.
664 *Natural Hazards and Earth System Sciences*, 16(10), 2259–2271. <https://doi.org/10.5194/nhess-16-2259-2016>
- 665
666 Lumbrazo, C., Bennett, A., Currier, W. R., Nijssen, B., & Lundquist, J. (2022). Evaluating
667 Multiple Canopy-Snow Unloading Parameterizations in SUMMA With Time-Lapse
668 Photography Characterized by Citizen Scientists. *Water Resources Research*, 58(6), 1–22.
669 <https://doi.org/10.1029/2021WR030852>
- 670
671 Lundberg, A., & Hallidin, S. (1994). Evaporation of intercepted snow: Analysis of govern-
672 ing factors. *Water Resources Research*, 30(9), 2587–2598. <https://doi.org/10.1029/94WR00873>
- 673
674 Lundquist, J. D., Dickerson-Lange, S., Gutmann, E., Jonas, T., Lumbrazo, C., & Reynolds, D. (2021). Snow interception modelling: Isolated observations have led to many land surface

- 675 models lacking appropriate temperature sensitivities. *Hydrological Processes*, 35(7), 1–20.
676 <https://doi.org/10.1002/hyp.14274>
- 677 MacDonald, J. P. J. (2010). *Unloading of intercepted snow in conifer forests* (Master of
678 Science August, University of Saskatchewan; pp. 0–93). <http://hdl.handle.net/10388/etd-09302010-145706>
- 680 Mahat, V., & Tarboton, D. G. (2014). Representation of canopy snow interception, unloading
681 and melt in a parsimonious snowmelt model. *Hydrological Processes*, 28(26), 6320–6336.
682 <https://doi.org/10.1002/hyp.10116>
- 683 Moeser, D., Stähli, M., & Jonas, T. (2015). Improved snow interception modeling using
684 canopy parameters derived from airborne LiDAR data. *Water Resources Research*, 51(7),
685 5041–5059. <https://doi.org/https://doi.org/10.1002/2014WR016724>
- 686 Musselman, K. N., Pomeroy, J. W., & Link, T. E. (2015). Variability in shortwave irradiance
687 caused by forest gaps: Measurements, modelling, and implications for snow energetics.
688 *Agricultural and Forest Meteorology*, 207, 69–82. <https://doi.org/https://doi.org/10.1016/j.agrformet.2015.03.014>
- 690 Nock, C. A., Lecigne, B., Taigourdeau, O., Greene, D. F., Dauzat, J., Delagrange, S.,
691 & Messier, C. (2016). Linking ice accretion and crown structure: towards a model
692 of the effect of freezing rain on tree canopies. *Annals of Botany*, 117(7), 1163–1173.
693 <https://doi.org/https://doi.org/10.1093/aob/mcw059>
- 694 Pfister, R., & Schneebeli, M. (1999). Snow accumulation on boards of different sizes and
695 shapes. *Hydrological Processes*, 13(14-15), 2345–2355. [https://doi.org/https://doi.org/10.1002/\(SICI\)1099-1085\(199910\)13:14/15%3C2345::AID-HYP873%3E3.0.CO;2-N](https://doi.org/https://doi.org/10.1002/(SICI)1099-1085(199910)13:14/15%3C2345::AID-HYP873%3E3.0.CO;2-N)
- 697 Pomeroy, J. W., Brown, T., Fang, X., Shook, K. R., Pradhananga, D., Armstrong, R., Harder,
698 P., Marsh, C., Costa, D., Krogh, S. A., Aubry-wake, C., Annand, H., Lawford, P., He,
699 Z., Kompanizare, M., & Moreno, J. I. L. (2022). The cold regions hydrological modelling
700 platform for hydrological diagnosis and prediction based on process understanding. *Journal
701 of Hydrology*, 615(128711), 1–25. <https://doi.org/10.1016/j.jhydrol.2022.128711>
- 702 Pomeroy, J. W., Fang, X., & Ellis, C. R. (2012). Sensitivity of snowmelt hydrology in Marmot
703 Creek, Alberta, to forest cover disturbance. *Hydrological Processes*, 26(12), 1891–1904.

- 704 https://doi.org/10.1002/hyp.9248
- 705 Pomeroy, J. W., Marsh, P., & Gray, D. M. (1997). Application of a distributed blowing snow
706 model to the arctic. *Hydrological Processes*, 11(11), 1451–1464. https://doi.org/10.1002/
707 (sici)1099-1085(199709)11:11%3C1451::aid-hyp449%3E3.0.co;2-q
- 708 Pomeroy, J. W., Parviainen, J., Hedstrom, N., & Gray, D. M. (1998). Coupled modelling of
709 forest snow interception and sublimation. *Hydrological Processes*, 12(15), 2317–2337. https:
710 //doi.org/10.1002/(SICI)1099-1085(199812)12:15%3C2317::AID-HYP799%3E3.0.CO;2-X
- 711 Pomeroy, J. W., & Schmidt, R. A. (1993). The Use of Fractal Geometry in Modelling Inter-
712 cepted Snow Accumulation and Sublimation. *Eastern Snow Conference*, 50, 231–239.
- 713 R Core Team. (2024). *R: A Language and Environment for Statistical Computing*. R Foun-
714 dation for Statistical Computing. https://www.r-project.org/
- 715 Rittger, K., Raleigh, M. S., Dozier, J., Hill, A. F., Lutz, J. A., & Painter, T. H. (2020). Canopy
716 Adjustment and Improved Cloud Detection for Remotely Sensed Snow Cover Mapping.
717 *Water Resources Research*, 56(6), n/a. https://doi.org/10.1029/2019WR024914
- 718 Roesch, A., Wild, M., Gilgen, H., & Ohmura, A. (2001). A new snow cover fraction parame-
719 terization for the ECHAM4 GCM. *Climate Dynamics*, 17(12), 933–946. https://doi.org//
720 10.1007/s003820100153
- 721 Safa, H., Krogh, S. A., Greenberg, J., Kostadinov, T. S., & Harpold, A. A. (2021). Unraveling
722 the Controls on Snow Disappearance in Montane Conifer Forests Using Multi-Site Lidar.
723 *Water Resources Research*, 57(12), 1–20. https://doi.org/10.1029/2020WR027522
- 724 Satterlund, D. R., & Haupt, H. F. (1967). Snow catch by Conifer Crowns. *Water Resources
725 Research*, 3(4), 1035–1039. https://doi.org/https://doi.org/10.1029/WR003i004p01035
- 726 Schmidt, R. A., & Pomeroy, J. W. (1990). Bending of a conifer branch at subfreezing temper-
727 atures: implications for snow interception. *Canadian Journal of Forest Research*, 20(8),
728 1251–1253. https://doi.org/10.1139/x90-165
- 729 Schmidt, R. A., & Troendle, C. A. (1989). Snowfall into a forest and clearing. *Journal of
730 Hydrology*, 110(3-4), 335–348. https://doi.org/10.1016/0022-1694(89)90196-0
- 731 Smith, C. D. (2007). Correcting the wind bias in snowfall measurements made with a Geonor
732 T-200B precipitation gauge and alter wind shield. *87th AMS Annual Meeting*.

- 733 Staines, J., & Pomeroy, J. W. (2023). Influence of forest canopy structure and wind flow
734 on patterns of sub-canopy snow accumulation in montane needleleaf forests. *Hydrological*
735 *Processes*, 37(10), 1–19. <https://doi.org/10.1002/hyp.15005>
- 736 Storck, P., Lettenmaier, D. P., & Bolton, S. M. (2002). Measurement of snow interception
737 and canopy effects on snow accumulation and melt in a mountainous maritime climate,
738 Oregon, United States. *Water Resources Research*, 38(11), 1–16. <https://doi.org/10.1029/>
739 2002wr001281
- 740 Troendle, C. A. (1983). The Potential for Water Yield Augmentation From Forest Management
741 in the Rocky Mountain Region. *Journal of the American Water Resources Association*,
742 19(3), 359–373. <https://doi.org/10.1111/j.1752-1688.1983.tb04593.x>
- 743 Valante, F., David, J. S., & Gash, J. H. C. (1997). Modelling interception loss for two sparse
744 eucalypt and pine forests in central Portugal using reformulated Rutter and Gash analytical
745 models. *Journal of Hydrology*, 190(1-2), 141–162. [https://doi.org/10.1016/S0022-1694\(96\)03066-1](https://doi.org/10.1016/S0022-1694(96)03066-1)
- 747 Van Stan, J. T., Siegert, C. M., Levia, D. F., & Scheick, C. E. (2011). Effects of wind-
748 driven rainfall on stemflow generation between codominant tree species with differing crown
749 characteristics. *Agricultural and Forest Meteorology*, 151(9), 1277–1286. <https://doi.org/>
750 10.1016/j.agrformet.2011.05.008
- 751 Varhola, A., Coops, N. C., Weiler, M., & Moore, R. D. (2010). Forest canopy effects on
752 snow accumulation and ablation: An integrative review of empirical results. *Journal of*
753 *Hydrology*, 392(3-4), 219–233. <https://doi.org/10.1016/j.jhydrol.2010.08.009>
- 754 Vionnet, V., Mortimer, C., Brady, M., Arnal, L., & Brown, R. (2021). Canadian historical
755 Snow Water Equivalent dataset (CanSWE, 1928–2020). *Earth System Science Data*, 13(9),
756 4603–4619. <https://doi.org/https://doi.org/10.5194/essd-13-4603-2021>
- 757 Watanabe, S., & Ozeki, J. (1964). Study of fallen snow on forest trees (II). Experiment on the
758 snow crown of the Japanese cedar. *Jap. Govt. Forest Exp. Sta. Bull*, 169, 121–140.
- 759 Wheeler, K. (1987). *Interception and redistribution of snow in a subalpine forest on a storm-*
760 *by-storm basis*. Western Snow Conference. <http://sites/westernsnowconference.org/PDFs/>
761 1987Wheeler.pdf